

Accepted Manuscript

Title: Heteroatom-induced band-reconstruction of metal vanadates for photocatalytic cyclohexane oxidation towards KA-oil selectivity

Authors: Liping Xiang, Jingjing Fan, Wenzhou Zhong, Liqui Mao, Kuiyi You, Dulin Yin



PII: S0926-860X(19)30071-7
DOI: <https://doi.org/10.1016/j.apcata.2019.02.015>
Reference: APCATA 16985

To appear in: *Applied Catalysis A: General*

Received date: 30 August 2018
Revised date: 30 January 2019
Accepted date: 9 February 2019

Please cite this article as: Xiang L, Fan J, Zhong W, Mao L, You K, Yin D, Heteroatom-induced band-reconstruction of metal vanadates for photocatalytic cyclohexane oxidation towards KA-oil selectivity, *Applied Catalysis A, General* (2019), <https://doi.org/10.1016/j.apcata.2019.02.015>

This is a PDF file of an unedited manuscript that has been accepted for publication. As a service to our customers we are providing this early version of the manuscript. The manuscript will undergo copyediting, typesetting, and review of the resulting proof before it is published in its final form. Please note that during the production process errors may be discovered which could affect the content, and all legal disclaimers that apply to the journal pertain.

Heteroatom-induced band-reconstruction of metal vanadates for photocatalytic cyclohexane oxidation towards KA-oil selectivity

Liping Xiang^a, Jingjing Fan^a, Wenzhou Zhong^{*,a}, Liqiu Mao^a, Kuiyi You^b, Dulin Yin^a

^aNational & Local United Engineering Laboratory for New Petrochemical Materials & Fine Utilization of Resources, Key Laboratory of Chemical Biology Traditional Chinese Medicine Reserach Ministry of Education, College of Chemistry and Chemical Engineering, Hunan Normal University, Changsha 410081, P. R.

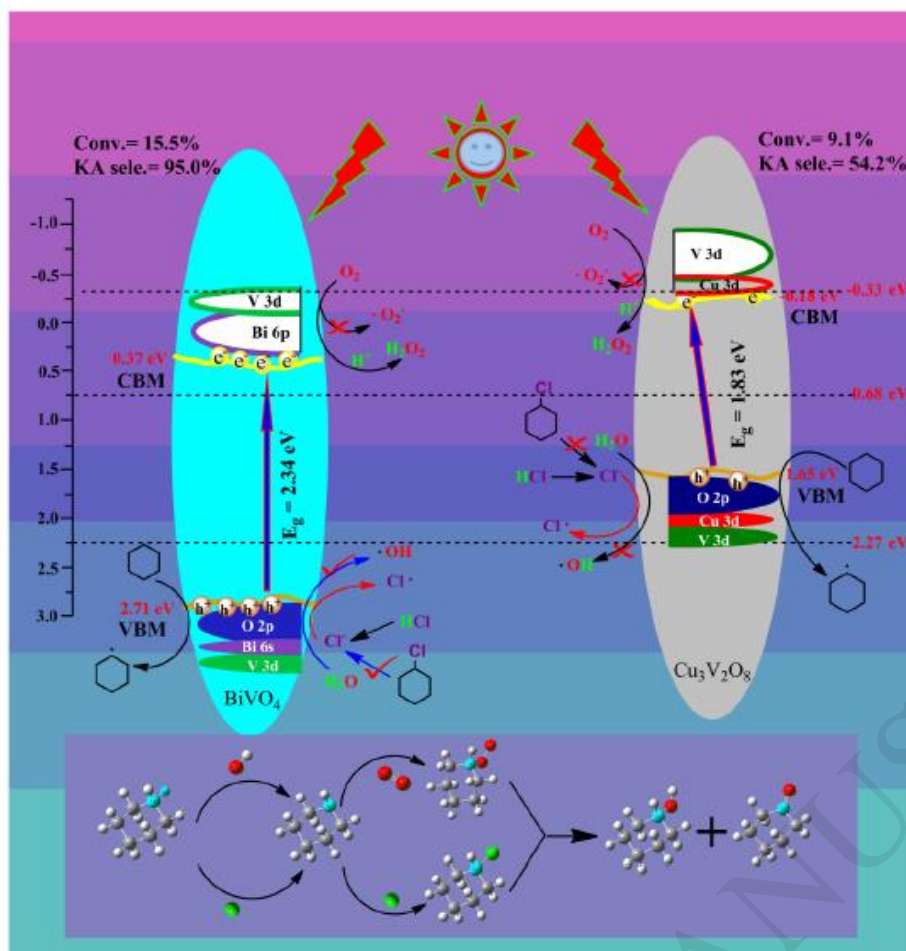
^bCollege of Chemical Engineering, Xiangtan University, Xiangtan 411105, PR China

*Corresponding authors: Wenzhou Zhong

Fax: +86-731-88872531; Tel.: +86-731-88872576

E-mail:zwenz79@163.com (W. Zhong)

Graphical Abstract



Highlights

- ► d^0 -Vanadate shows superior visible-light responsiveness.
- ► Heteroatom-tuning vanadates can alter the competitive reaction pathways.
- ► Electronic structure of vanadates interface to various reaction intermediates change.
- ► BiVO_4 promotes the oxidation with the higher TOF (7.5 h^{-1}) than $\text{Cu}_3\text{V}_2\text{O}_8$ (2.8 h^{-1}).
- ► A different KA-oil selectivity is obtained for BiVO_4 (95%) and $\text{Cu}_3\text{V}_2\text{O}_8$ (54%).

Abstract

Structure-function correlation constitutes a central theme in the selective photocatalytic oxidation of cyclohexane with molecular oxygen, as a result of precise tailoring band-structure towards KA-oil selectivity. Herein, we comparatively and systematically investigate the correlation among optical properties, electronic structure, and photocatalytic performance of two d^0 -vanadate photocatalysts (BiVO_4 and $\text{Cu}_3\text{V}_2\text{O}_8$) using theoretical calculations and experimental techniques. Results show that BiVO_4 promotes the selective oxidation pathway under visible-light irradiation with higher efficiency ($\text{TOF}=7.5 \text{ h}^{-1}$, based on the molar amount of V sites) and chemoselectivity (cyclohexanone/cyclohexanol molar ratio =3.0) than the $\text{Cu}_3\text{V}_2\text{O}_8$. Meanwhile, the photocatalytic performance of BiVO_4 demonstrates high photocatalytic selectivity towards KA-oil (95%), while $\text{Cu}_3\text{V}_2\text{O}_8$ seems to facilitate the accommodation of chlorine promoters, leading to very different chlorocyclohexane selectivity (46%). Such the distinct photocatalytic performances of BiVO_4 and $\text{Cu}_3\text{V}_2\text{O}_8$ can be ascribed to their unique electronic structures to facilitate the e^- - h^+ charge carriers and generation of reactive species during photoirradiation. The $\text{Bi}^{3+} 6p$ states of BiVO_4 are predominant components of the conduction band minimum (CBM) and hybridize with $\text{Bi}^{3+} 6s$, and $\text{O}^{2-} 2p$ and $\text{V}^{5+} 3d$ orbitals at the valence band maximum (VBM); whereas the $\text{Cu}^{2+} 3d$ and $\text{V}^{5+} 3d$ orbitals contribute to the CBM of $\text{Cu}_3\text{V}_2\text{O}_8$, and $\text{Cu}^{2+} 3d$, $\text{O}^{2-} 2p$ and $\text{V}^{5+} 3d$ orbitals at the VBM. So BiVO_4 with s-p matrix elements is more effective than the $\text{Cu}_3\text{V}_2\text{O}_8$ in producing $\cdot\text{OH}$, h^+ and H_2O_2 , which can rapidly oxidize the C-Cl bond cleavage for chlorocyclohexane intermediate to regenerate newly $\text{Cl}\cdot$ radicals in the next cycle reactions. Heteroatom-tuning of photocatalytic performance is further supported by universal evidences from experimental results by replacing Bi or Cu of the above vanadates with Ag, La, Sr, Fe or Ti atom and the study of the electrons, holes and radicals mediated reaction pathway by scavengers, respectively.

Keywords: Cyclohexane; Photocatalytic oxidation; Visible light; Structure-function correlation;

Electronic structure

1. Introduction

Direct insertion of molecule oxygen in aliphatic C–H bond is one of the most challenging and promising subjects from industrial and synthesis standpoints due to the high level of activation required [1, 2]. Catalytic and selective C–H bond functionalization of cyclohexane to KA-oil (a mixture of cyclohexanone and cyclohexanol) is a commercial procedure in the chemical industry as the KA-oil is an irreplaceable intermediate in the manufacture of nylon-6 and nylon-6, 6 polymers [3]. Owing to the intrinsic inertness of C–H bonds (dissociation energy=439 kJmol⁻¹), modern industrial oxidation of cyclohexane to KA-oil via the conventional thermocatalytic process has to be conducted under drastic conditions (1.5~3 MPa, 130~160 °C) in the presence of soluble based-cobalt or manganese catalysts, which leads to high energy consumption and a large amount of undesirable byproducts [4]. More importantly, maintaining a higher KA-oil selectivity at moderate under elevated heating conditions to high conversion rates is very difficult in view of the susceptibility of cyclohexane and KA-oil via the C–C bond cleavage to be completely oxidized to CO₂ and H₂O in the presence of oxygen. With these facts, given the demand for a green and sustainable transformation with fewer or even zero byproducts, the construction of an environmentally benign thermocatalytic-free oxidation process under mild conditions is highly desirable.

Photocatalytic reactions have received enormous attention not only for its potential applications in environmental treatment [5, 6], but also for organic synthesis of various valuable chemicals [7, 8]. In recent year, considerable efforts on energy shortage have been devoted to the design of photocatalytic oxidation systems alternative to the existing on the C–H bond thermo-activation of cyclohexane, with the aim of high efficiency of cyclohexane oxidation. Particularly, getting a high KA-oil production (e.g., less total oxidation products, CO₂) under ambient conditions has been intensively investigated with various photocatalysts such as semiconductor oxides [9], copper(II) chloride [10], transition metal complexes [11] and NaY zeolite [12]. Among the various photocatalytic oxidations, bulk TiO₂ with wide band gap energy (3.0–3.2 eV) constitutes a paradigmatic example of catalysts for the oxidative C–H activation of cyclohexane under UV-light irradiation [13]. However, undesired subsequently overoxidation or mineralization of cyclohexanone to CO₂ is essentially correlated with the photocatalytic decomposition over TiO₂ due to the production of highly oxidizing radicals such as surface lattice •O₂⁻ or O₃⁻ [14, 15]. To obtain an enhanced photocatalytic selectivity of TiO₂, increasing concerns on promoting the formed cyclohexanone desorption and inhibiting highly oxidizing •O₂⁻ production have focused on the

modification of the surface or bulk properties of TiO₂ materials. The groups of Madras reported that the Ag-substituted TiO₂ exhibited a cyclohexane conversion of 9% with a 63% cyclohexanone selectivity in chloroform medium under UV-light irradiation [16]. Mul *et al.* showed that the UV-light-driven photooxidation of cyclohexane with surface silylated-TiO₂ led a 95% selectively (conversion <1%) to cyclohexanone [17]. Among them, it is also reasonable to expect that the formation of heterojunction structures between a narrow band gap materials and TiO₂ can efficiently extend the photosensitivity of TiO₂ into the visible region. Ide *et al.* developed a FeO/TiO₂-catalyzed visible-light-induced photocatalytic oxidation of cyclohexane into KA-oil (conversion <1%; KA-oil selectively >99.9%) under a CO₂ atmosphere [18]. Shiraishi *et al.* designed TiO₂/rGO hybrid catalyst, which enhances the activity (conversion <0.5%; 83% KA-oil selectivity) to about twice that of bare TiO₂ [15]. Han and co-workers found that V₂O₅/TiO₂ exhibited the high photocatalytic activity (18% conversion) with a single selectivity to KA-oil at 2.0 MPa oxygen pressures [19]. All these reports suggest that rational designing of hetero-atom to TiO₂-containing materials probably produces a multiple heterojunction structure with modified photocatalytic activity. However, the photocatalytic activities with high partial oxidation selectivity in the visible-light region are insufficient under ambient conditions. Meanwhile, the relationship between electronic structure and photocatalytic performance towards KA-oil selectivity has been rarely studied, although over 20 photocatalysts have been discovered for cyclohexane photo-oxidation.

From the viewpoint of electronic state strategy, the transition metal V in +5 valence state possesses the same electronic configuration of Ti⁴⁺, but its 3d orbital is usually located below the analogous d orbitals of the Ti⁴⁺ in the energy spectrum and lowers the CBM to a more positive position [20]. Accordingly, V⁵⁺ should be considered to be one of potential core metal ions for visible-light photocatalyst. Although some literatures have reported that V⁵⁺ deposited on the different supports such as TS-1 [21], TiO₂ [19], C₃N₄ [22] and molybdophosphoric acids [23] can enhance the photocatalytic activity under visible-light irradiation, no photocatalysts based on core metal vanadium have been found for cyclohexane photo-oxidation. Especially, critical issue is the oxidizing ability of photogenerated hot holes within vanadium, which is thought to be much milder than that of hot holes in the valence band for most semiconductor photocatalysts [24], giving a possibility for the application in selective C–H bond activation. At present, some vanadates based on core metal vanadium such as BiVO₄, InVO₄, AgVO₄ and Zn₃V₂O₈ have been developed successfully as visible-light photocatalysts for the photocatalytic degradation of dye molecules [25], water

splitting [26] and CO₂ conversion [27]. In addition, these vanadates also allows a large change in the crystal morphology and new band structure, because atomic arrangement is expected to form and contribute to some new properties. Rational design and heteroatom tuning of electronic structure of photocatalysts, therefore, have become one of the most effective strategies to control their photocatalytic activity, which is also evident in several photocatalytic processes. For example, Fan and his co-workers investigated the effect of three crystalline phases of BiVO₄ on the degradation of methyl blue aqueous solution, and monoclinic BiVO₄ had the highest photocatalytic activity [28]. Cao *et al.* investigated TiO₂/vanadates (Sr₁₀V₆O₂₅, Ni₃V₂O₈, Zn₂V₂O₇) heterostructure photocatalysts for photoreduction of CO₂ into CH₄ under visible light irradiation, and revealed that TiO₂/Sr₁₀V₆O₂₅ could perform as an excellent photocatalytic material [29]. On the basis of the aforementioned considerations, so this family of vanadates provides opportunities to design new efficient photocatalysts for controlling cyclohexane oxidation towards KA-oil selectivity. Further, it will be clear whether the heteroatom-induced band-reconstruction would alter the competitive reaction pathways towards KA oil? If yes, what are its implications?

In the present study, we have chosen two d⁰-vanadate photocatalysts (BiVO₄ and Cu₃V₂O₈) by taking advantage of strong heteroatom-vanadate interactions to selectively modify the structure of photocatalyst. The special interactions between heteroatom and vanadate can introduce large electronic perturbations in electronic structure and induce obvious variations in crystal structure, which directly affects the catalytic performance. Cyclohexane selective oxidation on heteroatom-tuning vanadate catalysts is systematically evaluated under visible-light irradiation. When the heteroatoms are tuned, the electronic structures of vanadates interface to various reaction intermediates change. This response enables the significant tuning of the photo-catalysts selectivity, whereas the overall photo-catalytic activity is much less affected. A combination of comparative experiments and electronic band structure calculations for the vanadate photocatalysts can provide insights into the structure-function relationships: how the catalytic performance of vanadate catalysts for cyclohexane oxidation can be fine-tuned.

2. Experimental

2.1. Catalyst preparation

The monoclinic BiVO₄ was prepared via a simple precipitation method. In a typical procedure, 5 mmol Bi(NO₃)₃·5H₂O was dissolved in 30 mL HNO₃ (1.5 M), and 5 mmol NH₄VO₃ was added to

5 mL of 15% $\text{NH}_3 \cdot \text{H}_2\text{O}$. Then, the above solutions were mixed together under stirring, and the pH value was adjusted to 7 by 15% $\text{NH}_3 \cdot \text{H}_2\text{O}$. The resulting suspension was stirred for 3 h at room temperature. The yellow precipitate was collected and washed with ethanol and deionized water three times each, and dried at 80 °C in air for 6 h.

For the synthesis of $\text{Cu}_3\text{V}_2\text{O}_8$, 5 mmol $\text{Cu}(\text{NO}_3)_2 \cdot 3\text{H}_2\text{O}$ was dissolved in 50 mL deionized water. Then, a 50 mL NH_4VO_3 solution (0.1 M), which was prepared by dissolving NH_4VO_3 into deionized water at 80 °C for 5 min, was slowly added to the $\text{Cu}(\text{NO}_3)_2$ solution under vigorous stirring and the mixture was stirred for about 2 h. The precursor was collected and washed with ethanol and deionized water three times each, and dried at 80 °C in air for 12 h. The final product was obtained by calcination at 500 °C in air for 2 h. In addition, TiVO_4 , SrVO_4 , CrVO_4 , LaVO_4 , CoVO_4 , AlVO_4 and FeVO_4 were prepared by a similar procedure.

For the sake of comparison, single-metal oxides (Bi_2O_3 , V_2O_5 and CuO) were prepared by calcination of the corresponding salts ($\text{Bi}(\text{NO}_3)_3 \cdot 5\text{H}_2\text{O}$, NH_4VO_4 and $\text{Cu}(\text{NO}_3)_2 \cdot 3\text{H}_2\text{O}$) at 500 °C for 8 h.

2.2. Characterization techniques

The crystalline phase of the samples was analyzed with a Bruker D8 Advance X-ray diffractometer using $\text{CuK}\alpha$ radiation ($\lambda=1.542 \text{ \AA}$). Transmission electron microscopy (TEM) images and high-resolution transmission electron microscopy (HR-TEM) images were obtained by using a JEOL-2010 TEM with an acceleration voltage of 200 kV. Raman spectra of samples were analyzed with a Renishaw in Via Raman Microscope system with a 514.5 nm laser source and a spectral resolution of 0.3 cm^{-1} . The optical properties of the samples were analyzed by diffuse reflectance UV-vis spectra using a Varian-Cary 5000 spectrometer with BaSO_4 as a reference material. Surface composition and surface states of samples were determined by X-ray photoelectron spectroscopy (XPS) using an Imaging Photoelectron Spectrometer (Axis Ultra, Kratos Analytical Ltd.) with Al Ka radiation (1486.7 eV). Binding energies were corrected with reference to the C 1s peak of adventitious carbon (binding energy = 284.8 eV); fit XPS software was used for curve fitting. Photoluminescence measurement was performed using a JASCO FP-6500 type fluorescence spectrophotometer with an excitation wavelength of 290 nm light at room temperature.

2.3. DFT calculations

All our calculations were performed based on the plane-wave pseudopotential method using the

CASTEP code. The generalized gradient approximation (GGA) with Perdew-Burke-Ernzerhof (PBE) functional was adopted for the exchange-correlation potential [30]. Hubbard-like potential U was employed to better treat exchange and correlation associated with the localized d-states of the Cu and V cations for $\text{Cu}_3\text{V}_2\text{O}_8$ [31]. The plane-wave energy cutoff was set to 400 eV. A Monkhorst-Pack k-points grid of $2 \times 4 \times 4$ and $2 \times 2 \times 4$ was set for sampling in the first Brillouin zone during geometry optimizations of BiVO_4 and $\text{Cu}_3\text{V}_2\text{O}_8$, respectively. The atomic coordinates and the shape of the cell were allowed to fully relax, until the residual forces on all atoms, the stresses on the cell, and the convergence tolerance for self-consistent energy were less than 0.01 eV/Å, 0.05 GPa, 0.001 Å, and 10^{-5} eV, respectively. The electronic structure calculation was performed using the optimized geometric structure.

2.4. Photocatalytic reactions

Photocatalytic selective oxidation of cyclohexane into KA-oil was performed using a self-designed photochemical reactor equipped with a water-cooling jacket, which was connected with a oxygen gas burette to monitor the gas uptake in our previously published work (Fig S1) [21]. The photoreactor consisted of a jacketed quartz tube of 3.8 cm i.d. and 20 cm length and an inside reactor of 1.5 cm i.d. and 19 cm length. A 20 W tungsten-bromine lamp (light intensity, 275 $\text{mW} \cdot \text{cm}^2$) with an UV light filter (Osram brand) was immersed in a mixture of acetonitrile (5 mL), cyclohexane (5 mmol), concentrated HCl (0.1 mL) and 50 mg photocatalyst. After being filled with the desired amount of oxygen (1 atm), the reaction suspension was vigorously stirred to eliminate the influence of mass transfer. Owing to the heating effect of light irradiation illuminated, the temperature of reaction solution could maintain at 28–30 °C. After illumination reaction, the mixture was centrifuged to completely remove the catalyst particles. The liquid products were quantitatively analyzed by an Agilent 6890N gas chromatograph equipped with flame ionization detector and a DB-17 polysiloxane capillary column (30 m \times 0.32 mm \times 0.50 μm) using n-hexanol as an internal standard. The gas products were analyzed by gas chromatography equipped with a TCD detector. All products were satisfactorily identified by comparing the MS spectra with those of the authentic samples. All raw materials and products were established carbon mass balances. All the experiments were repeated at least 4 times in parallel to obtain an average value.

3. Results and discussion

3.1. Crystal structure and morphology

The crystal structure and phase compositions of the materials are investigated by XRD analysis.

As shown in Fig. 1, the peaks of BiVO_4 located at 28.82° , 30.55° , 34.50° , 35.22° , 39.78° , 42.47° , 46.71° , 47.31° , 50.32° and 53.25° are attributed to the diffractions of the (121), (040), (200), (002), (211), (051), (240), (042), (202) and (161) crystal planes of monoclinic BiVO_4 (JCPDS No. 00-014-0688) [32], respectively. Interesting, $\text{Cu}_3\text{V}_2\text{O}_8$ material structured by strong Cu^{2+} -vanadate interactions has a similar phase by comparison with BiVO_4 . The peaks at 2θ values of 15.0° , 18.7° , 26.8° , 27.3° , 30.8° , 32.2° , 36.1° , 37.0° , 37.7° , 38.6° , 45.2° and 58.5° are distinctly indexed to the (100), (-110), (021), (111), (-211), (012), (-212), (130), (-131), (102), (040) and (-330) crystal planes of $\text{Cu}_3\text{V}_2\text{O}_8$ with a monoclinic phase (JCPDS No. 26-0567) [33], respectively. Compared with the XRD patterns of the CuO (JCPDS No. 48-1548), Bi_2O_3 (JCPDS No. 27-0050) and V_2O_5 (JCPDS No. 41-1246), no other peaks for impurity are observed for BiVO_4 and $\text{Cu}_3\text{V}_2\text{O}_8$, which confirms the high purity of the resultant metal vanadates in phase composition. Further, Fig. 6 (A_0 and B_0) shows schematic crystal structures of BiVO_4 and $\text{Cu}_3\text{V}_2\text{O}_8$. The crystal structure of $\text{Cu}_3\text{V}_2\text{O}_8$ consists of the V–O tetrahedra and Cu–O octahedra, while the monoclinic phase BiVO_4 is composed of the V–O tetrahedra and Bi–O polyhedra. We think that the Bi^{3+} cation in the polyhedral field with the electronic states is obviously different from the Cu^{2+} cation in the octahedral field, which should impose significant effects on the electronic structure and photocatalytic activities of the studied metal vanadates.

The crystal structures of BiVO_4 and $\text{Cu}_3\text{V}_2\text{O}_8$ are investigated by TEM and HR-TEM analysis (Fig. 2). Evidently, BiVO_4 exhibits a worm-like morphology with an average diameter of 50 nm. The obvious contrast between the dark edge and the pale center confirms that the BiVO_4 contains hollow spheres, and the average diameter of hollow spheres is approximately 30-90 nm. Interesting, TEM image of $\text{Cu}_3\text{V}_2\text{O}_8$ clearly shows that the individual sphere of $\text{Cu}_3\text{V}_2\text{O}_8$ is also porous hollow sphere with an average diameter of 30-150 nm, but the wall is comprised of loosely packed aggregates of irregular flakiness. Obviously, the morphology of these metal vanadates is different from that of the corresponding the single-metal oxides (Bi_2O_3 , V_2O_5 and CuO), as shown in Fig. S2. In addition, the corresponding HR-TEM image of BiVO_4 reveals that the lattice distances of 0.309 nm and 0.475 nm match those of the (110) and (121) planes of monoclinic BiVO_4 [34]. A different lattice distance of 0.363 nm is found in $\text{Cu}_3\text{V}_2\text{O}_8$, attributed to the (-211) plane of $\text{Cu}_3\text{V}_2\text{O}_8$. These lattice distances can be clearly seen in the corresponding HR-TEM image, indicating that the BiVO_4 and $\text{Cu}_3\text{V}_2\text{O}_8$ possess a good crystallization, respectively.

3.2. Surface properties and band gap energy

The incorporation of heteroatom into the vanadates solid has, therefore, important effects on the local structure surrounding the core V atoms. The structural information of BiVO₄ and Cu₃V₂O₈, with the single-metal oxides (Bi₂O₃, V₂O₅ and CuO) from the Raman spectra is shown in Fig. 3. Compared with the corresponding single-metal oxides (Fig. 3B), the vibrational characteristic Raman peaks at 126, 209, 247, 326, 363, 758 and 825 cm⁻¹ are the clear signature of the typical vibrations of monoclinic BiVO₄ (Fig. 3A) [34-36]. The peaks at 126 and 209 cm⁻¹ correspond to the external modes (rotation/ translation) of BiVO₄. The peaks at 326 and 363 cm⁻¹ are ascribed to the asymmetric (B_g bending) and symmetric (A_g bending) deformation modes of the VO₄³⁻ tetrahedron due to a strong interaction between Bi³⁺ and VO₄³⁻, respectively. The intense peak at 824 cm⁻¹ is attributed to a symmetric V–O stretching mode with A_g symmetry, along with a weak shoulder at about 758 cm⁻¹ assigned to an antisymmetric V–O stretching mode with B_g symmetry. In addition, the peak at 247 cm⁻¹ relates to the Bi–O symmetric stretching in a deformation mode of BiO₈ dodecahedron and at 209 cm⁻¹ corresponds to the vibration of the crystal lattice (external modes), respectively. In contrast, Raman peak pattern of Cu₃V₂O₈ by strong Cu²⁺-vanadate interactions, however, is obviously different from that of BiVO₄ sample. The peak intensities of deformation VO₄³⁻ modes are greatly decreased, which can be explained on the basis of the packing of the crystal structure. (Fig. 3A) [36]. Furthermore, a positive shift in the vibrational mode of V–O has been observed, which suggests that the V–O bond length of Cu₃V₂O₈ is disturbed by the formation of the V–O–Cu linkages. This is also indicative of the presence of the bending of the same structural motif or a breaking of the total symmetry of the VO₄³⁻ structure [37, 38], which is confirmed by the above theoretical studies. Such a similar phenomenon was earlier predicted by Colón *et al.*, on Cu-doped TiO₂ catalysts [39]. Therefore, it is clear from the figure that the Raman study provides the valuable information on the structural variations by incorporation of heteroatoms into vanadates. However, it is unclear the electronic structure difference of the as-prepared composites and in what state the heteroatom remains into the vanadates lattice. Further, we conducted XPS test to analyze the changes of valence state of elements and binding energy.

For comparison, the XPS spectra of the BiVO₄ and Cu₃V₂O₈ are exposed in Fig. 4. The full surface survey XPS spectrum given in Fig. 4A reveals the presence of Bi, V, O and C elements in BiVO₄ sample and Cu, V, O and C elements in Cu₃V₂O₈ sample, confirming that other metals and impurities are not present. The appearance of C is atmospheric in origin. The high resolution XPS spectrum of Bi for BiVO₄ shows the binding energies of Bi 4f located at 164.6 and 159.0 eV

corresponding to the Bi 4f_{7/2} and Bi 4f_{5/2} (Fig. 4B), respectively, which can be assigned to Bi³⁺ valence state of the composites [40]. Meanwhile, the curve of V 2p displays two strong peaks centering at about 516.0 and 524.1 eV, which is attributed to the binding energy of V 2p_{3/2} and V 2p_{1/2} respectively, indicating that V species exist in +5 valence state for BiVO₄ samples (Fig. 4D) [41]. Interesting, a binding energy shift of V 2p_{3/2} and V 2p_{1/2} for Cu₃V₂O₈ toward higher binding energy at 516.7 and 524.6 eV takes place compared with BiVO₄ (due to the different electronegativities of Bi³⁺ and Cu²⁺), indicating that the electron cloud density is reduced. This may be ascribed to the strong electrostatic attraction of Cu²⁺, influencing the local chemical state of V⁵⁺ species. That is to say, to achieve local charge balance in the Cu₃V₂O₈ lattice, some of the V ions may acquire higher oxidation state by releasing electrons, which is consistent with the structural variations in spectroscopic (Raman) studies. In addition, as shown in Fig. 4C, the binding energy of the Cu 2p_{3/2} (934.33 eV) and Cu 2p_{1/2} (955.1 eV) peaks, together with the strong satellite peaks in the range of 940–945 eV [42], indicates that Cu²⁺ is the dominant valence state for Cu₃V₂O₈. A weak component (3%) at 931.59 eV, associated with the presence of Cu⁺, is observed after deconvolution of Cu 2p_{3/2} peak [42]. Therefore, one more convincing follow up is the gap states in the forbidden band, which is formed due to the introduction of Cu⁺ states. Thus, electrons present in the gap states of forbidden band can be excited to the conduction band by means of a wide range of energy. This facilitates the elongation of light absorption into the visible region, which is further confirmed by the following UV-vis spectra. From the observation in O 1s spectra (Fig. 4E), the resolved O 1s peaks located at 529.1 and 531.2 eV are assigned to O–V and O–Bi bonds of BiVO₄ [43], while peaks at 529.2 and 531.5 eV are ascribed to O–V and O–Cu entities of Cu₃V₂O₈, respectively. Obviously, the peak of O–V slightly shifted toward a higher binding energy value of about 0.10 eV for Cu₃V₂O₈, further suggesting that there is strengthening of O–V bond with a modified bonding state. As a result, the differences in the intensities and peak position of the peaks in the Raman and XPS spectra clearly demonstrate the variations in the local crystal structure of the vanadates samples, as the packing of the structure related to the interactive forces between the heteroatom and VO₄³⁻ cations is directly related to the electronic transitions in the materials. In order to further understand the change of band structure after heteroatom-doping, we determined the position of VBM. As shown in Fig. 4F, the VBM value of BiVO₄ and Cu₃V₂O₈ is 2.71 and 1.65 eV, respectively, which is in line with the following calculated value of VBM by the empirical formula $E_{VB} = E_{CB} + E_g$. This suggests that the presence of heteroatom causes band-reconstruction of metal

vanadates and its influence on KA-oil selectivity.

To understand the variation of the optical bandgap upon the change in the substitution of metal atom in the vanadates, the UV-vis absorption spectra of BiVO₄ and Cu₃V₂O₈, with the single-metal oxides (Bi₂O₃, V₂O₅ and CuO) are analyzed using UV-vis spectroscopy, as shown in Fig. 5A. Comparison of all the BiVO₄ and Cu₃V₂O₈ photocatalysts spectra with those of referent single-metal oxides, both of BiVO₄ and Cu₃V₂O₈ generally exhibit a strong absorption from UV-light to visible-light region, implying the possibility of visible-light photocatalytic activity over these samples. Compared with the absorption edge of BiVO₄, Cu₃V₂O₈ has a red shift from 500 to 540 nm, suggesting that the Cu₃V₂O₈ can absorb longer wavelength light. Moreover, an apparent absorption hump with an extrapolated absorption edge at about 750 nm is appeared for Cu₃V₂O₈, which is associated with the Cu²⁺ d–d orbital intraband transition in the octahedral field. In addition, band-gap energy is calculated by the formula $\alpha hv = A(hv - E_g)^{n/2}$, where h , α , v , E_g and A are the Planck constant, the absorption coefficient, light frequency, band gap and proportionality constant, respectively [44]. Among them, the n value depends on the type of electronic transition: $n = 2$ for a direct transition; $n = 0.5$ for indirect transition. Based on the following theory calculation results (Fig. 6), the electronic transitions of BiVO₄ and Cu₃V₂O₈ are direct and indirect, respectively. As a result, the E_g of BiVO₄ can be calculated from the plot of $(\alpha hv)^2$ versus (hv) and founded to be about 2.34 eV, whereas that of Cu₃V₂O₈ can be estimated from the plot of $(\alpha hv)^{1/2}$ versus (hv) and founded to be about 1.83 eV (Figs. 5B and 5C). Further, the conduction band (CB) for vanadates can be also calculated by the equation: $E_{CB} = \chi - E^e - 0.5E_g$, in which E_{CB} , χ , E^e and E_g are the CB potential, the geometric mean of the absolute electronegativities of the constituent atoms (the absolute electronegativity of an individual atom is the arithmetic mean of the atomic electron affinity and the first ionization energy [45]), the free electron energy on the hydrogen scale (~4.5 eV), and the vanadate band gap energy [46-48]. Additionally, the value of E_{VB} can be obtained by $E_{VB} = E_{CB} + E_g$. Thus, the CBs for BiVO₄ and Cu₃V₂O₈ are calculated to be 0.37 and -0.18 eV, and the VBs for BiVO₄ and Cu₃V₂O₈ are calculated to be 2.71 and 1.65 eV, respectively.

3.3 DFT simulated electronic and optical properties

Aiming at exploring the impact of heteroatom-tuning on the crystal structure and electronic structure of metal vanadates, the full PBE calculations are performed for the unique light absorption and photocatalysis properties presented by the BiVO₄ and Cu₃V₂O₈ catalyst. As shown in Table 1, the optimized cell constants of BiVO₄ and Cu₃V₂O₈ reproduce very well the experimental data [49,

50], and this variation of lattice parameters may be associated with the different ionic radii of the Cu^{2+} and Bi^{3+} cations. The average V–O bond length calculated is 1.740 Å in BiVO_4 and 1.980 Å in $\text{Cu}_3\text{V}_2\text{O}_8$, and less V–O bond length will lead to form a more dispersive band. The Bi–O bond length in BiVO_4 is obviously larger than the Cu–O bond length in $\text{Cu}_3\text{V}_2\text{O}_8$, which makes the crystal field of $\text{Cu}_3\text{V}_2\text{O}_8$ stronger than that of BiVO_4 . Figs. 6A and 6B show the calculated electronic band structures for the BiVO_4 and $\text{Cu}_3\text{V}_2\text{O}_8$, respectively. BiVO_4 has an indirect and minimum energy gap of 2.22 eV, along with two direct and only slightly larger energy gaps (2.28 eV and 2.29 eV) at the A point (-0.5, 0, 0) and Z point (0, -0.5, 0.5). Usually, the direct band gap is favorable to recombine photogenerated electrons and holes in the semiconductors, which indicates that these two narrow and direct energy gaps for BiVO_4 should mainly contribute to the high photocatalytic activity in the visible light region [51]. In comparison, the indirect energy gap is observed for $\text{Cu}_3\text{V}_2\text{O}_8$, which is consistent with the experimental and previous theoretical results [52]. However, it is noted that all of the calculated band gaps are generally smaller than the corresponding experimental values due to the well-known LDA error, which is only expected to provide a rather approximate description of the band gaps and excited [53].

Fig. 7 shows the total and site-projected density of states (DOS). Obviously, the CBM of BiVO_4 is mainly contributed by the Bi^{3+} 6*p* and V^{5+} 3*d* states, whereas the CBM of $\text{Cu}_3\text{V}_2\text{O}_8$ is composed primarily of the V^{5+} 3*d* and Cu^{2+} 3*d* states. Similarly, the lowest unoccupied molecular orbital (LUMO) of BiVO_4 is predominantly composed of Bi^{3+} 6*p*, V^{5+} 3*d* and O^{2-} 2*p* orbitals. However, the LUMO of $\text{Cu}_3\text{V}_2\text{O}_8$ mainly derives from the hybridization of V^{5+} 3*d* and Cu^{2+} 3*d* orbitals. As we known, it will be useful to have more p-character in the CBM to avoid recombination in photocatalytic reactions, when the VBM mainly consists of oxygen p-orbitals [54]. Thus, Bi^{3+} contributes the p-character of BiVO_4 in the stability of the electrons in the CBM by reduction of recombination rates of excited charges. The partial density of states of individual elements in BiVO_4 show that the contribution of the Bi^{3+} 6*s* lone pair plays an important role in the construction of VBM with a dispersive band structure (Fig. 7A), which contributes in decreasing the effective mass of electrons and improves the photocatalytic activity of photocatalysts [55]. Further, the contribution of the Bi^{3+} 6*p* orbitals to the CBM of BiVO_4 is about 10%, whereas Cu^{2+} 6*p* accounts for only 0.4% of the orbital formation, indicating that BiVO_4 processes a strong covalent feature of the Bi–O and V–O bonds. This shows that more electrons should transfer from Bi (or V) to adjacent oxygen atoms rather than being shared between Bi (or V) and oxygen atoms, facilitating the charge separation of

photogenerated carriers and thus benefiting the photocatalytic performance [56]. On the other hand, the VBM structures of photocatalysts are also quite different (Figs. 7A and 7B). The VBM of BiVO₄ is mainly composed of O²⁻ 2*p*, Bi³⁺ 6*s* and V⁵⁺ 3*d* orbitals, whereas the VBM of Cu₃V₂O₈ is dominated by O²⁻ 2*p*, Cu²⁺ 3*d* and V⁵⁺ 3*d* character. As a result, Bi³⁺ 6*s* mixed with O²⁻ 2*p* orbitals dominate the HOMO of BiVO₄; whereas Cu²⁺ 3*d* mixed with O²⁻ 2*p* orbitals dominate the HOMO of Cu₃V₂O₈. So the potential for valence band top of BiVO₄ is different from that of Cu₃V₂O₈, which is required for the photocatalytic oxidation of organic compounds in the presence of oxygen. Based on the PDOS, the unoccupied Cu 3*d* states contribute to the lowest VB bottom of Cu₃V₂O₈, resulting in that the visible-light absorption of Cu₃V₂O₈ with the narrowest band gap is the strongest (which is confirmed by the XPS and UV-vis spectra analysis).

3.4 Photocatalytic oxidation of cyclohexane

Photocatalytic activity of the as-synthesized vanadates are evaluated to establish how the extent of heteroatom-tuning for vanadates can exert an influence on the photooxidation of cyclohexane into KA-oils in the presence of concentrated HCl as an additive under visible light irradiation, as shown in Table 2. No product is detected in the control experiments without catalyst or light irradiation, which indicates that the cyclohexane oxidation is truly driven by a photocatalytic process (entry 1). Similar visible light stimulation of pure V₂O₅ as a core metal element results in a considerable photocatalytic activity for cyclohexane oxidation in CH₃CN, which is due to the fact that fast electron-hole recombination is the dominant process under these experimental conditions (entry 2). In contrast, as shown by entries 5–6, BiVO₄ and Cu₃V₂O₈ structured by heteroatom-vanadate interactions remarkably enhance visible light photocatalytic activity for the KA-oil formation, indicating that the modification of the crystal and electronic structure in the metal vanadate is responsible for the increasing visible light absorption performance. To compare the intrinsic activity of vanadium species in the different metal vanadate, turnover frequency (TOF) toward selective formation of KA oils is calculated for cyclohexane conversion based on V sites on catalyst. BiVO₄ catalyst successfully and repeatedly displays a high TON value of 7.5 h⁻¹, giving 15.5% cyclohexane conversion and 95.0% KA-oil selectivity (cyclohexanone/cyclohexanol molar ratio =3.0). Compared with BiVO₄, Cu₃V₂O₈ catalyst shows a relative low TON value of 2.8 h⁻¹, giving 9.1% cyclohexane conversion and 54.2% KA-oil selectivity (cyclohexanone/cyclohexanol molar ratio =1.3). The decrease in KA-oil selectivity may be mainly due to less further photo-oxidation of the formed chlorocyclohexane intermediate to the re-formation of KA-oils via secondary reactions, since the

BiVO_4 catalyst is different from $\text{Cu}_3\text{V}_2\text{O}_8$ in generation of interactive intermediates (such as electrons, holes and $\bullet\text{OH}$) for the cleavage of C–Cl bond of chlorocyclohexane to re-form radical $\text{Cl}\bullet$ species. Actually, the reactive $\text{Cl}\bullet$ as highly effective species to capture H atom of cyclohexane in the photocatalysis cycling of BiVO_4 and $\text{Cu}_3\text{V}_2\text{O}_8$, is further confirmed by compared to that without the additive HCl (entries 7 and 8). Moreover, the additive concentrated HBr instead of concentrated HCl is investigated as a possible reference (entry 9). No photo-catalysis efficiency, however, is obtained under similar conditions, revealing that the $\text{Cl}\bullet$ generated in entries 5 and 6 can undergo reversible chlorine-atom transfer with carbon-centered radicals. This is likely because the Br atom formed is no easy to capture H atom of cyclohexane due to its low activity and the cleavage of C–Br bond is also difficult in the existence of high Br free radicals [57]. These catalytic activities of metal vanadates by the substitution of Bi^{3+} ions for Cu^{2+} demonstrate not only the close correlations between photocatalytic abilities and generation of interactive intermediates and charge carriers.

To understand why the substituting of metal element into the framework of vanadates is able to enhance its photocatalytic activity significantly, other metal vanadates such as TiVO_4 , SrVO_4 , CrVO_4 , LaVO_4 , CoVO_4 , AlVO_4 and FeVO_4 are also prepared and submitted to the oxidation reaction (Table 2). Among different metal vanadates, the substituting of Co^{2+} , Fe^{3+} and Al^{3+} into the vanadate framework is also an effective method to improve visible photocatalytic activity on oxidation of cyclohexane into KA-oils (entries 14–16), and a high KA-oil selectivity of 93.1% can be obtained for AlVO_4 . In contrast, TiVO_4 , SrVO_4 , CrVO_4 and LaVO_4 show much less photocatalytic activity (entries 10–13). Interesting, TiVO_4 exhibits the highest cyclohexanol/cyclohexanone molar ratio value of 4.1 among all metal vanadates, giving a 77.6% cyclohexanol selectivity. These results show that the catalytic activities of metal vanadates appear to be closely related to its heteroatom-induced band-reconstruction, as above discussed in the differences of BiVO_4 and $\text{Cu}_3\text{V}_2\text{O}_8$. This further indicates that the selective cyclohexane oxidation towards KA-oils selectivity can be tuned using heteroatom-tuning electronic structure.

Perhaps the compelling evidence regarding the singular nature of the BiVO_4 and $\text{Cu}_3\text{V}_2\text{O}_8$ catalyst can be obtained from the different behavior of the product evolution in the cyclohexane photo-oxidation. To study this, the product distributions measured with the BiVO_4 and $\text{Cu}_3\text{V}_2\text{O}_8$ catalyst at different time intervals is shown in Fig. 8. A similar low conversion of cyclohexane is observed for BiVO_4 and $\text{Cu}_3\text{V}_2\text{O}_8$ after irradiation for 0.5 h, and then the level of cyclohexane conversion increases linearly with an increasing irradiation time from 0.5 to 8 h. A possible

explanation for this phenomenon is a similar radicalic-type autoxidation process with the BiVO_4 or $\text{Cu}_3\text{V}_2\text{O}_8$ as catalyst. Interesting, for the BiVO_4 catalyst the cyclohexane conversion rate initially is the higher under visible-light irradiation, implying a higher utilization efficiency of visible-light. However, the evolution of the rates of formation of cyclohexanone, cyclohexanol and chlorocyclohexane are remarkably different during the cyclohexane photo-oxidation process. For the BiVO_4 and $\text{Cu}_3\text{V}_2\text{O}_8$ catalyst, the increased cyclohexanone formation rate and decreased cyclohexanol formation rate are appeared for prolonged reaction times, indicating that the products are formed in parallel and cyclohexanol formed initially can be transformed to cyclohexanone via a sequential oxidation process as the reaction proceeds. As a comparison, the formation rate and ketone/alcohol molar ratio, however, exceed that of $\text{Cu}_3\text{V}_2\text{O}_8$ used. In addition, for BiVO_4 catalyst, the chlorocyclohexane formation rate initially increases, reaching a maximum (16.9%) after irradiation for 1 h and smoothly decreasing to 6.7% (3 h); whereas the $\text{Cu}_3\text{V}_2\text{O}_8$ catalyst initially shows a slight decrease for the chlorocyclohexane formation rate, but after 2 h the formation rate always remains “frozen” in that state, independent of the irradiation time. The analysis of dependences of the formation rates of KA-oil and chlorocyclohexane confirms that KA-oil is formed by reversible chlorine-atom transfer process. To find out the other reaction intermediates, we took aliquots of the sample at regular intervals and analyzed them by iodometric titration. No peroxides such as hydroperoxide and cyclohexyl hydroperoxide are detected, indicating that the peroxide intermediates can be quickly decomposed into the active radicals by catalysts under irradiation conditions.

3.5 Photocatalytic reactive species

Molecular oxygen plays a major role in photocatalytic selective oxidations elicited by photocatalyst, because molecular oxygen is involved in the generation of reactive species (such as h^+ , $\bullet\text{O}_2^-$, $\text{Cl}\bullet$ and $\bullet\text{OH}$) and driving catalytic reactions. Electronic structures and optical properties of the photocatalysts, therefore, will have significant effects on the photocatalytic activity by tailoring reactive species production. As a result, trapping experiments for both BiVO_4 and $\text{Cu}_3\text{V}_2\text{O}_8$ are conducted to trace the different active species in cyclohexane photocatalysis. The scavengers (10 mmol/L) triethanolamine (TEOA), benzoquinone (BQ), dimethylbutadiene (DMBD) and isopropanol (IPA) are used to trap holes (h^+), superoxide anion radicals ($\bullet\text{O}_2^-$), halogen ($\text{Cl}\bullet$) and hydroxyl radicals ($\bullet\text{OH}$), respectively [58-60]. As shown in Table 3, introducing TEOA into the photocatalytic system causes the BiVO_4 photocatalyst to quickly deactivate, confirming that

photogenerated h^+ is the mainly active species in BiVO_4 sample during the selective oxidation of cyclohexane. However, scavenger of h^+ for $\text{Cu}_3\text{V}_2\text{O}_8$ has less opportunity to take part in photocatalytic oxidation process (entry 1). This is attributed to the fact that the lone pair of electrons of N element of TEOA can combine with the empty d-orbitals of the transition metal Bi element of photocatalysts to form strong covalent bonds. Differently, when IPA is added into the photocatalytic reaction solution, cyclohexane conversion decreases from 15.5% to 5.8% and 9.1% to 7.7% for BiVO_4 and $\text{Cu}_3\text{V}_2\text{O}_8$, respectively (entry 2); therefore, it is concluded that $\bullet\text{OH}$ takes part in the selective oxidation reaction and BiVO_4 photocatalyzes more production of hydroxyl radical compared to $\text{Cu}_3\text{V}_2\text{O}_8$. By contrast, no obvious change is observed on the photo-oxidation of cyclohexane with the introduction of p-benzoquinone into catalytic system (entry 3), indicating that the less $\bullet\text{O}_2^-$ radicals produce for BiVO_4 and $\text{Cu}_3\text{V}_2\text{O}_8$ under visible light irradiation. In addition, a low photoconversion of cyclohexane into KA-oil is also obtained with the addition of DMBD into the photocatalytic reaction solution (entry 4), revealing that the formed $\text{Cl}\bullet$ radicals from Cl^- oxidation are expected to efficiently initiate the same chain process by abstraction of hydrogen from cyclohexane under our conditions.

As is well known, the photogenerated electrons (e^-) are another key reactive species in photocatalytic reaction because e^- can produce $\bullet\text{O}_2^-$ and $\bullet\text{OH}$. Therefore, we used the AgNO_3 (1 mM) to trap e^- generating from BiVO_4 and $\text{Cu}_3\text{V}_2\text{O}_8$ photocatalysts, because the separated electrons are used up in making metallic silver. Interesting, the higher cyclohexane photoconversion is observed over BiVO_4 under visible light irradiation (Table 3, entry 5), implying that the scavenger of e^- for BiVO_4 has less opportunity to join recombination of electron-hole pairs and produces more holes to take part in reaction process. In this case, the $\bullet\text{OH}$ radicals generated in BiVO_4 photocatalyst system are not from photogenerated electrons, but from photogenerated holes. Further, the remarkably different photocatalytic performance of the BiVO_4 photocatalyst, compared with that of $\text{Cu}_3\text{V}_2\text{O}_8$, can be also ascribed to the different charge carriers trapping, migration and separation efficiency. Photoluminescence emission spectroscopy (PL) is carried out to investigate the transfer and fate of photoinduced carriers: the lower PL intensity generally represents the higher separation capacity of charge carriers in semiconductor-based systems, resulting in a higher photocatalytic activity [61]. Obviously, a strong emission peak at about 520 nm is observed for the $\text{Cu}_3\text{V}_2\text{O}_8$ photocatalyst (Fig. 9), demonstrating that the electrons and holes over the $\text{Cu}_3\text{V}_2\text{O}_8$ can facilely recombine. By contrast, the relatively low PL intensity of BiVO_4 implies that BiVO_4 can migrate the photogenerated

electrons and holes more effectively, with inhibiting the recombination of charge carriers. The discovery by the PL spectra is an evidence for the previous Raman spectroscopy study and crystal structure analysis in that the activity is tuned by the V–O bond length of VO_4^{3-} for metal vanadates. We have proved that the average V–O bond length of VO_4^{3-} tetrahedron in BiVO_4 is 1.74 Å, and it is obviously shorter than that of $\text{Cu}_3\text{V}_2\text{O}_8$ catalyst. Based on the results of Shannon *et al.*, the electron delocalization of the metal-oxygen bond in oxides easily occurs in the reduced metal-oxygen bond length in comparison to metal oxides [62]. Therefore, increased electron delocalization of the short V–O bond for BiVO_4 will increase effective transfer of charge carriers, and then lead to the enhanced photocatalytic activity.

3.6 Photocatalytic reaction mechanism

The above results provide the direct evidence for that (i) BiVO_4 and $\text{Cu}_3\text{V}_2\text{O}_8$ distinctly differ in photo-generation of reactive species. BiVO_4 can photocatalyze more production of $\bullet\text{OH}$, h^+ , H_2O_2 and $\text{Cl}\bullet$, and (ii) processes a higher separation capacity of charge carriers than $\text{Cu}_3\text{V}_2\text{O}_8$. These observations are well predicted by the energy band structures of BiVO_4 and $\text{Cu}_3\text{V}_2\text{O}_8$. Under irradiation of light, BiVO_4 and $\text{Cu}_3\text{V}_2\text{O}_8$ are excited simultaneously and the electrons (e^-) in the VB can be excited to the CB with the generation of the same amount of holes (h^+) on VB in both BiVO_4 and $\text{Cu}_3\text{V}_2\text{O}_8$. The normal photoexcitation in $\text{Cu}_3\text{V}_2\text{O}_8$ is from the hybridization state of $\text{V}^{5+} 3d$ and $\text{Cu}^{2+} 3d$ orbitals to the hybridization state of $\text{Cu}^{2+} 3d$ and $\text{O}^{2-} 2p$ orbitals. However, $\text{Bi}^{3+} 6s$ states are predominant components of the bottom of the CB and hybridize with $\text{O}^{2-} 2p$ and $\text{V}^{5+} 3d$, and $\text{Bi}^{3+} 3p$ and $\text{V}^{5+} 3d$ orbitals at the bottom of the VB for the BiVO_4 . The values of s–p matrix elements are big, which contributes in reducing recombination rates of excited charges with achieving the better separation of the photogenerated electron-hole pairs for the BiVO_4 . The separation capacity of charge carriers is well consistent with its remarkably low PL intensity (Fig. 9). In addition, the CB level of BiVO_4 (0.37 eV/NHE) and $\text{Cu}_3\text{V}_2\text{O}_8$ (–0.18 eV/NHE) is more positive than the redox potential of $\text{O}_2/\bullet\text{O}_2^-$ (–0.33 eV/NHE) [63], the electrons located on the CB of BiVO_4 and BiVO_4 cannot reduce O_2 to yield O_2^- via single-electron transfer routes ($\text{O}_2 + \text{e}^- = \bullet\text{O}_2^-$). The reduction of O_2 to product H_2O_2 via a two-electron process [$\text{O}_2 + 2\text{e}^- + 2\text{H}^+ = \text{H}_2\text{O}_2$ (aq)], however, can occur on BiVO_4 and $\text{Cu}_3\text{V}_2\text{O}_8$, which can be attributed to the fact that the CB levels of BiVO_4 and $\text{Cu}_3\text{V}_2\text{O}_8$ are more negative compared to the redox potential of $\text{O}_2/\text{H}_2\text{O}_2$ (0.68 eV/NHE) and $\text{H}_2\text{O}_2/\bullet\text{OH}$ (0.71 eV/NHE) [24]. In contrast, for BiVO_4 with a strong covalent feature of the Bi–O and V–O bonds, the more electrons can be transfer by Bi→O or (V→O) rather than being shared, and the formed intensified

local electric field at the BiVO_4 surface can promote the transfer of trapped hot electrons to adsorbed O_2 and Cl^- , therefore benefiting more production of $\bullet\text{OH}$ and $\text{Cl}\bullet$. Furthermore, based on the scavenger reactivity in trapping experiments (Table 3), one can conclude that h^+ and $\bullet\text{OH}$ are the major active species in the photocatalytic oxidation of cyclohexane by using BiVO_4 catalysts. At the same time, the more photo-induced holes can also oxidize H_2O to form $\bullet\text{OH}$ radicals, because the VB level (+2.71 eV/NHE) of BiVO_4 is also sufficiently positive than the $\bullet\text{OH}/\text{H}_2\text{O}$ potential (+2.27 eV/NHE) [64]. In addition, these photo-induced holes can also oxidize cyclohexane and Cl^- to form cyclohexyl and $\text{Cl}\bullet$ radicals, which are expected to initiate the same chain process by abstraction of hydrogen from cyclohexane. The addition of DMBD as scavengers into the reaction solution provides evidence that $\text{Cl}\bullet$ radicals are involved in the photocatalytic oxidation process (Table, entry 4). Therefore, these results imply that the $\bullet\text{OH}$, $\text{Cl}\bullet$ and cyclohexyl radicals are the mainly active species for the selective oxidation of cyclohexane to KA-oil. In contrast, based on the obtained active species trapping experiments, the photocatalytic reaction might involve more electrons as reactive species for the production of the above radicals through the oxidation pathway by using $\text{Cu}_3\text{V}_2\text{O}_8$ catalyst.

According to the experimental and theoretical investigation, some promising photooxidation processes and mechanisms are proposed for the different photocatalytic activities, as shown in Fig. 10 and Fig. S3. Visible light promotes photoexcitation of metal vanadate to produce the VB holes (h^+) and CB electrons (e^-) (Eq. (1)). Then the CB electrons are captured by water molecule in the acidic solution to product H_2O_2 via a two-electron process, and H_2O_2 can be further reduced to hydroxyl radicals ($\bullet\text{OH}$) by electron trapped in the CB (only for BiVO_4 photocatalyst). In addition, the formed holes can react with H_2O molecules to produce $\bullet\text{OH}$ radicals; these $\bullet\text{OH}$ radicals further react with water to yield hydroxyl radical-water complexes (Eq. (2)). Meanwhile, cyclohexane is oxidized with the VB holes to cyclohexyl radical. This related to the large positive redox potential of VB holes and $\text{OH}\bullet$ radicals as opposed to the mild driving force for the chain initiation process with the production of cyclohexyl radical. Molecular oxygen cannot reduce to yield O_2^- , which is not effective in directly reacting with the C–H bond of cyclohexane, but can be captured by cyclohexyl radical to form a free cyclohexyl-peroxy radical (Eq. (4)). Subsequently, cyclohexyl peroxy radical couples by two cyclohexyl peroxy radicals to product KA-oil and O_2 , or is reduced to cyclohexanone by CB electrons; additionally, this radical can also react with vicinal cyclohexane to form another cyclohexyl radical for the next cycle reactions and cyclohexyl hydroperoxide. The latter (CyOOH)

mostly rearranges to cyclohexanone and water under photocatalytic conditions (Eq. (5)). In addition, another minor pathway via $\bullet\text{OH}$ radicals coupling with cyclohexyl radicals to product a cyclohexanol may also exist and all formed cyclohexanol may be subsequently oxidized to cyclohexanone by the VB holes or $\bullet\text{OH}$ radicals (Eq. (6)), resulting a high cyclohexanone/cyclohexanol molar ratio. It is confirmed that a small quantity of ionic chlorine exists in the acidic solution, showing a synergistic factor in accelerating the photocatalytic reaction, since the same experiment performed with addition of other Brønsted acids (such as HBr and H_2SO_4) and CCl_4 cannot obtain similar effects under photocatalytic conditions. This is possible for chlorine radicals from hydrochloric acid to be formed by the VB holes under visible light irradiation in that $\text{Cl}\bullet$ radicals are less energetic than $\text{OH}\bullet$ radicals (Eq. (3)) [65]. In addition, Cl^- may be oxidized with the VB holes to yield $\bullet\text{OH}$. Thus the $\text{Cl}\bullet$ radicals can effectively attack the C–H bond of cyclohexane by a chain transfer oxidation that is faster than the corresponding reaction with $\text{OH}\bullet$ radicals (Eq. (4)). However, it is also necessary for there to be present enough holes or $\text{OH}\bullet$ radicals for the oxidative cleavage of C–Cl band of chlorocyclohexane intermediate to regenerate newly $\text{Cl}\bullet$ radicals for the next cycle reactions (Eq. (7)), resulting in good stability. As a result, BiVO_4 processes a higher separation capacity of charge carriers than $\text{Cu}_3\text{V}_2\text{O}_8$, which leads to more production of photogenerated holes and $\text{OH}\bullet$ radicals under the same photo-radiation, resulting in a higher cyclohexane conversion and KA-oil selectivity simultaneously. This is due to the evidence that holes and $\text{HO}\bullet$ have more oxidizing power to convert to the complete oxidizing product cyclohexanone. This is not surprising, as high selectivity for chlorocyclohexane is usually observed in $\text{Cu}_3\text{V}_2\text{O}_8$ photocatalysts, which is further confirmed by the fact that the various reactive species after adding the scavengers are quite different under our experimental conditions. Interesting, no $\bullet\text{O}_2^-$ is formed via the reduction of O_2 by the photo-formed CB e^- on BiVO_4 and $\text{Cu}_3\text{V}_2\text{O}_8$, which is the key species for the cyclohexanone decomposition to CO_2 via the cleavage of C–C bond. Thus, the formed cyclohexanone is not subsequently decomposed to CO_2 by photocatalysis, leading to selective production of KA-oil.

4. Conclusion

In summary, metal vanadates have been proven to be a novel series of visible-light-driven photocatalysts for the efficient photooxidation of cyclohexane to KA-oil for the first time, along with the intermediate is obtained as the total oxidation product. Excellent partial oxidation KA-oil selectivity (95%) and efficiency ($\text{TOF}=7.5 \text{ h}^{-1}$) are achieved with 15.5% conversion using a BiVO_4

in oxygen under ambient conditions (room temperature and 1atm pressure). In more detail, BiVO₄ and Cu₃V₂O₈ vanadates, as tunable optical properties by incorporating metal Bi³⁺ or Cu²⁺ ions, are compared systematically for their abilities to generate reactive species and charge carriers toward selective oxidation pathways during photoexcitation. The formation of reactive species is found to highly depend on the crystal structure and surface electronic state of BiVO₄ and Cu₃V₂O₈ photocatalysts by experimental and theoretical studies. The construction of VBM and CBM positions by hybridization of Bi³⁺ 6*s* and 6*p* orbitals facilitates the direct trapping and mobility of hot electrons from the VBM to CBM for BiVO₄, promoting the generation of hydroxyl radical and H₂O₂ reactive species toward selective formation of KA oils. These atomic-level findings will provide valuable insights for understanding the photocatalytic mechanisms of the heteroatom-tuning vanadates for associated reactive species with their different trends in photocatalytic activation of aliphatic C–H bond.

Acknowledgments

This work was supported by the Natural Science Foundation of China (Grant No.21576078 and 21878074) and the Natural Science Foundation of Hunan Province (Grant No.2016JJ2081) and Innovation Platform Open Fund of Hunan College (16K052).

References

- [1] A. Henríquez, H.D. Mansilla, A.M. Martínez-de la Cruz, J. Freer, D. Contreras, *Appl. Catal. B: Environ.* 206 (2017) 252–262.
- [2] G. de Ruiter, K.M. Carsch, S. Gul, R. Chatterjee, N.B. Thompson, M.K. Takase, J. Yano, T. Agapie, *Angew. Chem. Int. Ed.* 56 (2017) 4772–4776.
- [3] U. Schuchardt, D. Cardoso, R. Sercheli, R. Pereira, R.S. da Cruz, M.C. Guerreiro, D. Mandelli, E.V. Spinacé, E.L. Pires, *Appl. Catal. A Gen.* 211 (2001) 1–17.
- [4] A.A. Alshehri, A.M. Alhanash, M. Eissa, M.S. Hamdy, *Appl. Catal. A Gen.* 554 (2018) 71–79.
- [5] L. Suhadolnik, A. Pohar, B. Likozar, M. Čeh, *Chem. Eng. J.* 303 (2016) 292–301.
- [6] A.A. Memon, A.A. Arbab, S.A. Patil, N. Mengal, K.C. Sun, I.A. Sahito, S.H. Jeong, H.S. Kim, *Appl. Catal. A Gen.* 566 (2018) 87–95.

- [7] J. Kou, C. Lu, J. Wang, Y. Chen, Z. Xu, R.S. Varma, *Chem. Rev.* 117 (2017) 1445–1514.
- [8] V. D.B.C. Dasireddy, B. Likozar, *J. Taiwan Inst. Chem. E.* 82 (2018) 331–341.
- [9] A. Maldotti, A. Molinari, R. Amadelli, *Chem. Rev.* 102 (2002) 3811–3836.
- [10] K. Takaki, J. Yamamoto, K. Komeyama, T. Kawabata, K. Takehira, *Bull. Chem. Soc. Jpn.* 77 (2004) 2251–2255.
- [11] A. Maldotti, A. Molinari, P. Bergamini, R. Amadelli, P. Battioni, D. Mansuy, *J. Mol. Catal. A* 113 (1996) 147–157.
- [12] H. Sun, F. Blatter, H. Frei, *J. Am. Chem. Soc.* 118 (1996) 6873–6879.
- [13] M.N. Lyulyukin, P.A. Kolinko, D.S. Selishchev, D.V. Kozlov, *Appl. Catal. B: Environ.* 220 (2018) 386–396.
- [14] P. Du, J.A. Moulijn, G. Mul, *J. Catal.* 238 (2006) 342–352.
- [15] Y. Shiraishi, S. Shiota, H. Hirakawa, S. Tanaka, S. Ichikawa, T. Hirai, *ACS Catal.* 7 (2017) 293–300.
- [16] R. Vinu, G. Madras, *Appl. Catal. A Gen.* 366 (2009) 130–140.
- [17] A.R. Almeida, J.T. Carneiro, J.A. Moulijn, G. Mul, *J. Catal.* 273 (2010) 116–124.
- [18] Y. Ide, H. Hattori, S. Ogo, M. Sadakane, T. Sano, *Green Chem.* 14 (2012) 1264–1267.
- [19] D. Yang, T. Wu, C. Chen, W. Guo, H. Liu, B. Han, *Green Chem.* 19 (2017) 311–318.
- [20] M. Oshikiri, M. Boero, J. Ye, Z. Zou, G. Kido, *J. Chem. Phys.* 117 (2002) 7313–7318.
- [21] W. Zhong, T. Qiao, J. Dai, L. Mao, Q. Xu, G. Zou, X. Liu, D. Yin, F. Zhao, *J. Catal.* 330 (2015) 208–221.
- [22] S. Verma, R.B. Nasir Baig, M.N. Nadagouda, R.S. Varma, *ACS Sustainable Chem. Eng.* 4 (2016) 2333–2336.
- [23] J. She, Z. Fu, J. Li, B. Zeng, S. Tang, W. Wu, H. Zhao, D. Yin, S.R. Kirk, *Appl. Catal. B: Environ.* 182 (2016) 392–404.
- [24] S. Samanta, S. Khilari, D. Pradhan, R. Srivastava, *ACS Sustainable Chem. Eng.* 5 (2017) 2562–2577.
- [25] A. Malathi, J. Madhavan, M. Ashokkumar, P. Arunachalam, *Appl. Catal. A Gen.* 555 (2018) 47–74.
- [26] D. Ke, T. Peng, L. Ma, P. Cai, P. Jiang, *Appl. Catal. A Gen.* 350 (2008) 111–117.
- [27] S. Gao, B. Gu, X. Jiao, Y. Sun, X. Zu, F. Yang, W. Zhu, *J. Am. Chem. Soc.* 139 (2017) 3438–3445.

- [28] H.M. Fan, T.F. Jiang, H.Y. Li, D.J. Wang, L.L. Wang, J.L. Zhai, D.Q. He, P. Wang, T.F. Xie, J. Phys. Chem. C 116 (2012) 2425–2430.
- [29] Y. Yan, Y. Yu, D. Wu, Y. Yang, Y. Cao, Nanoscale, 8 (2016) 949–958.
- [30] G. Kresse, D. Joubert, Phys. Rev. B 59 (1999) 1758–1775.
- [31] M. Yashima, R.O. Suzuki, Phys. Rev. B 79 (2009) 125201–125206.
- [32] X. Xu, S. Kou, X. Guo, X. Li, X. Ma, H. Mao, J. Phys. Chem. C 121 (2017) 16257–16265.
- [33] M. Li, Y. Gao, N. Chen, X. Meng, C. Wang, Y. Zhang, D. Zhang, Y. Wei, F. Du, G. Chen, Chem. Eur. J. 22 (2016) 1–9.
- [34] C. Yin, S. Zhu, Z. Chen, W. Zhang, J. Gu, D. Zhang, J. Mater. Chem. A 1 (2013) 8367–8378.
- [35] J. Yu, A. Kudo, Adv. Funct. Mater. 16 (2006) 2163–2169.
- [36] S.M. Thalluri, C.M. Suarez, M. Hussain, S. Hernandez, A. Virga, G. Saracco, N. Russo, Ind. Eng. Chem. Res. 52 (2013) 17414–17418.
- [37] T. Kawada, A. Ikematsu, T. Tajiri, S. Takeshima, M. Machida, Int. J. Hydrogen Energ. 40 (2015) 10726–10733.
- [38] K. Bhattacharyya, S. Varma, A. K. Tripathi, S.R. Bharadwaj, A.K. Tyagi, J. Phys. Chem. C 112 (2008) 19102–19112.
- [39] J.M. Valero, S. Obregón, G. Colón, ACS Catal. 4 (2014) 3320–3329.
- [40] J. Su, X.-X. Zou, G.-D. Li, X. Wei, C. Yan, Y.-N. Wang, J. Zhao, L.-J. Zhou, J.-S. Chen, J. Phys. Chem. C 115 (2011) 8064–8071.
- [41] M. Balamurugan, G. Yun, K.-S. Ahn, S.H. Kang, J. Phys. Chem. C 121 (2017) 7625–7634.
- [42] L. Zhou, Q. Yan, J. Yu, R.J.R. Jones, N. Becerra-Stasiewicz, S.K. Suram, A. Shinde, D. Guevarra, J.B. Neaton, K.A. Persson, J.M. Gregoire, Phys. Chem. Chem. Phys. 18 (2016) 9349–9352.
- [43] P.C.J. Graat, M.A.J. Somers, Appl. Surf. Sci. 100 (1996) 36–40.
- [44] L. Zhang, J. Zhou, C. Zhang, J. Mater. Chem. A 2 (2014) 14903–14907.
- [45] Q. Li, H. Meng, P. Zhou, Y.Q. Zheng, J. Wang, J.G. Yu, J.R. Gong, ACS Catal. 3 (2013) 882–889.
- [46] M. Butler, D. Ginley, J. Electrochem. Soc. 125 (1978) 228–232.
- [47] R.G. Pearson, Inorg. Chem. 27 (1988) 734–740.
- [48] Y.I. Kim, S.J. Atherton, E.S. Brigham, T.E. Mallouk, J. Phys. Chem. 97 (1993) 11802–11810.
- [49] X.-L. Wei, H. Zhang, G.-C. Guo, X.-B. Li, W.-M. Lau, L.-M. Liu, J. Mater. Chem. A 2 (2014)

2101–2109.

[50] P.J. Coing-Boyat, *Acta Cryst. B* 38 (1982) 1546–1548.

[51] Z. Zhao, Z. Li, Z. Zou, *Phys. Chem. Chem. Phys.* 13 (2011) 4746–4753.

[52] L. Zhou, Q. Yan, A. Shinde, D. Guevarra, P.F. Newhouse, N. Becerra-Stasiewicz, S.M. Chatman, J.A. Haber, J.B. Neaton, J.M. Gregoire, *Adv. Energy Mater.* 5 (2015) 1500968-1500980.

[53] R.W. Godby, M. Schlüter, L.J. Sham, *Phys. Rev. Lett.* 56 (1986) 2415–2418.

[54] S. Murugesan, M.N. Huda, Y. Yan, M.M. Al-Jassim, V. (Ravi) Subramanian, *J. Phys. Chem. C* 114 (2010) 10598–10605.

[55] A. Kudo, Y. Miseki, *Chem. Soc. Rev.* 38 (2009) 253–278.

[56] Z. Chen, P. Sun, B. Fan, Q. Liu, Z. Zhang, X. Fang, *Appl. Catal. B: Environ.* 170–171 (2015) 10–16.

[57] J.T. Wang, B.S. Zhang, Y.M. Wang, Q.M. Hu, *Organic Chemistry*, 2nd ed., Nankai University Press, Tianjing, 2002 (Chapter 2).

[58] G. Li, K.H. Wong, X. Zhang, C. Hu, J.C. Yu, R.C. Chan, P.K. Wong, *Chemosphere*, 76 (2009) 1185–1191.

[59] J. Cao, B. Xu, H. Lin, B. Luo, S. Chen, *Chem. Eng. J.* 185–186 (2012) 91–99.

[60] U.A. Joshi, J.R. Darwent, H.H.P. Yiu, M.J. Rosseinsky, *J. Chem. Technol. Biotechnol.* 86 (2011) 1018–1023.

[61] R. Georgekutty, M.K. Seery, S.C. Pillai, *J. Phys. Chem. C* 112 (2008) 13563–13570.

[62] R. Shannon, *Acta Crystallogr., Sect. A: Cryst. Phys., Diffr., Theor. Gen. Crystallogr.*, 32 (1976) 751–767.

[63] J. Kim, C.W. Lee, W. Choi, *Environ. Sci. Technol.* 44 (2010) 6849–6854.

[64] H.F. Cheng, B.B. Huang, Y. Dai, X.Y. Qin, X.Y. Zhang, *Langmuir* 26 (2010) 6618–6624.

[65] M. Lewandowski, D.F. Ollis, *J. Catal.* 217 (2003) 38–46.

Table 1. Calculated lattice parameters and previously reported experimental structure data for the BiVO₄ and Cu₃V₂O₈ samples.

Crystal structure	Theoretical calculation values		Experimental values		
	BiVO ₄	Cu ₃ V ₂ O ₈	BiVO ₄ ^d	Cu ₃ V ₂ O ₈ ^e	
Lattice parameters	$a/\text{Å}$	5.194	5.161	5.197	5.196
	$b/\text{Å}$	5.090	5.431	5.096	5.355
	$c/\text{Å}$	11.697	6.534	11.702	6.505
	α	90.00	69.07	90.00	69.22
	β	90.00	88.36	90.00	88.69
	γ	90.39	68.21	90.40	68.08
D_{V-O} ^a	Å	1.740	1.980	1.745	-
D_{M-O} ^b	Å	2.459	1.940	2.441	-

^aThe D_{V-O} represents the average bond length of V–O; ^b the D_{M-O} represents the average bond length of Bi–O and Cu–O for BiVO₄ and Cu₃V₂O₈, respectively; ^c the D_{O-O} represents the average bond length of O–O; ^d [36]; ^e [37].

Table 2 Visible light-driven oxidation of cyclohexane with molecular oxygen catalyzed by the different catalysts ^a.

Entry	Catalyst	Conversion (%) ^b	Selectivity (%) ^c				TOF (h ⁻¹) ^d
			KA-oil				
1	Blank	0	-	-	-	-	-
2	V ₂ O ₅	3.8	74.9	25.1	20.6	54.3	0.5
3	Bi ₂ O ₃	0.1	100	0	49.6	50.4	-
4	CuO	0.6	48.6	51.4	37.0	11.6	-
5	BiVO ₄	15.5	95.0	4.9	24.0	71.0	7.5
6	Cu ₃ V ₂ O ₈	9.1	54.2	45.8	23.1	31.1	2.8
7 ^e	BiVO ₄	0.3	100	-	27.4	72.6	0.2
8 ^e	Cu ₃ V ₂ O ₈	0.1	100	-	36.5	63.5	0.03
9 ^f	BiVO ₄	0.2	100	-	-	100	0.13
10	TiVO ₄	6.4	96.5	3.5	77.6	18.9	1.6
11	SrVO ₄	9.0	75.2	24.8	18.4	56.8	3.3
12	CrVO ₄	9.1	80.1	16.9	19.9	63.2	2.3
13	LaVO ₄	9.1	73.7	26.3	23.3	50.4	3.5
14	CoVO ₄	12.0	85.1	14.9	23.5	61.6	3.6
15	AlVO ₄	12.7	93.1	6.9	22.8	70.3	2.7
16	FeVO ₄	13.0	87.9	12.1	25.1	62.9	3.3

^a All reactions were done with 0.0050 g of catalyst, 4 mmol cyclohexane, O₂ (1 atm), 5 mL of acetonitrile, at 28-30 °C, time (8 h), concentrated HCl (0.1 ml) as an additive, tungsten-bromine lamp (20W) as visible light source.

^b Conversion (%) based on substrate = $\{1 - [(\text{concentration of substrate left after reaction}) \times (\text{initial concentration of substrate}) - 1]\} \times 100$; ^c Product selectivity = content of this product / (adding cyclohexane amount (mmol) - the amount of cyclohexane recovered (mmol)) $\times 100\%$.

^d Turnover frequency (TOF): number of moles of cyclohexane converted per the molar amount of V sites and hour of reaction time.

^e Without adding concentrated HCl as an additive in photo-oxidation system.

^f Using concentrated HBr as an acidic additive instead of concentrated HCl.

Table 3 Reactive species trapping experiments of BiVO₄ and Cu₃V₂O₈ samples.

Entry	Scavenger	BiVO ₄				Cu ₃ V ₂ O ₈			
		Conv. (%)	Sele. (%)			Conv. (%)	Sele. (%)		
									
1	TEOA	3.0	0	41.6	58.1	8.6	35.8	23.1	41.1
2	IPA	5.8	3.4	16.9	79.7	7.7	21.1	19.7	59.3
3	BQ	12.1	4.6	32.6	62.8	9.0	35.5	10.8	53.7
4	DMBD	0	-	-	-	0.5	50.5	43.5	6.0
5	AgNO ₃	13.6	5.0	19.5	75.5	6.1	35.7	17.8	46.5

Figure captions:

Fig. 1. XRD patterns of BiVO₄, Cu₃V₂O₈, Bi₂O₃, V₂O₅ and CuO samples.

Fig. 2. TEM images of BiVO₄ (A₀, A₁ and A₂) and Cu₃V₂O₈ samples (B₀, B₁ and B₂).

Fig. 3. Visible Raman spectra of (A) for BiVO₄ and Cu₃V₂O₈ samples and (B) for Bi₂O₃, V₂O₅ and CuO samples.

Fig. 4. XPS spectra of (A) survey, (B) Bi 4f, (C) Cu 2p, (D) V 2p, (E) O 1s and (F) valence band of BiVO₄ and Cu₃V₂O₈ samples

Fig. 5. UV-Vis spectra of (A) for BiVO₄, Cu₃V₂O₈, Bi₂O₃, V₂O₅ and CuO samples; Tauc plots of BiVO₄ (B) for direct band gap and Cu₃V₂O₈ for indirect band gap.

Fig. 6. Crystal structures of BiVO₄ (A₀) and Cu₃V₂O₈ (B₀) samples; band structures of BiVO₄ (A) and Cu₃V₂O₈ (B) samples.

Fig. 7. Total density of state of BiVO₄ (A₀) and Cu₃V₂O₈ (B₀) samples; partial density of state of BiVO₄ (A) and Cu₃V₂O₈ (B) samples.

Fig. 8. Effect of the irradiation time on the product evolution for BiVO₄ (A) and Cu₃V₂O₈ (B) samples. The error bars represent the standard deviations of three independent measurements of the same sample.

Fig. 9. Photoluminescence spectra with the excitation wavelength of 290 nm.

Fig. 10. Photooxidation processes of cyclohexane with O₂ vapor over the BiVO₄ and Cu₃V₂O₈ samples.

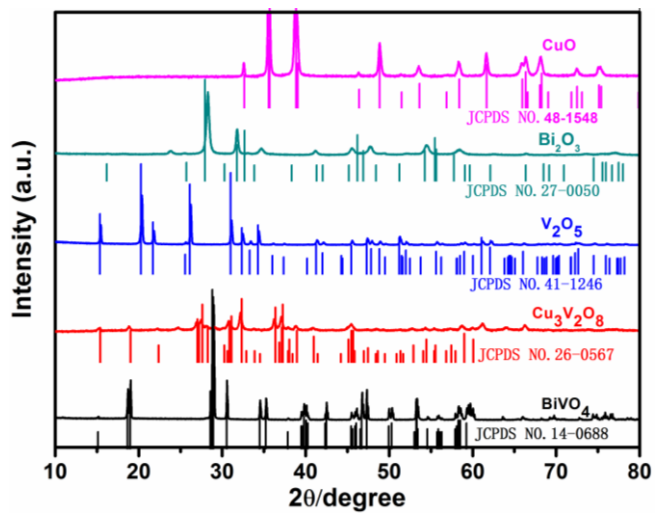


Fig. 1.

ACCEPTED MANUSCRIPT

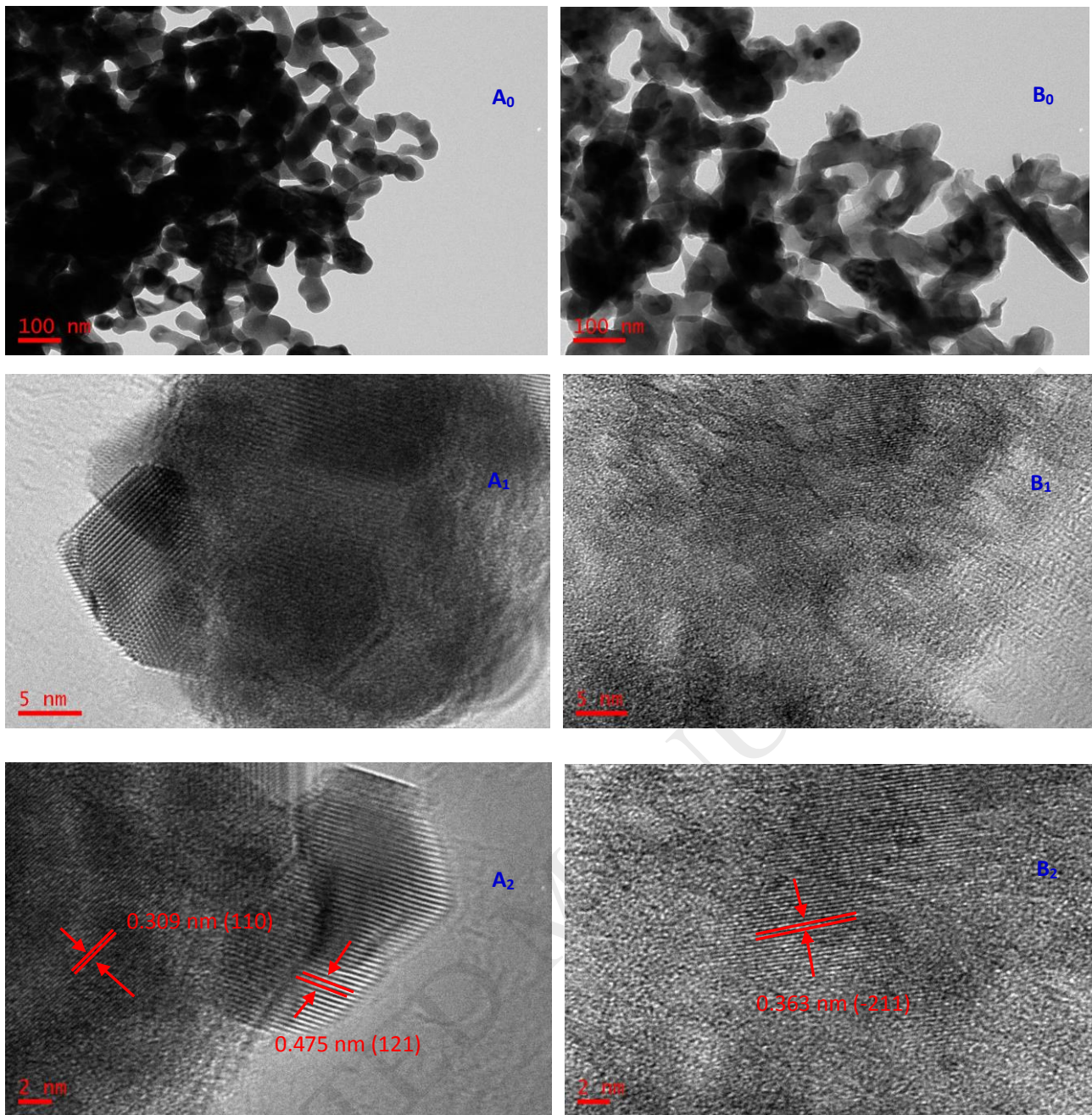


Fig. 2

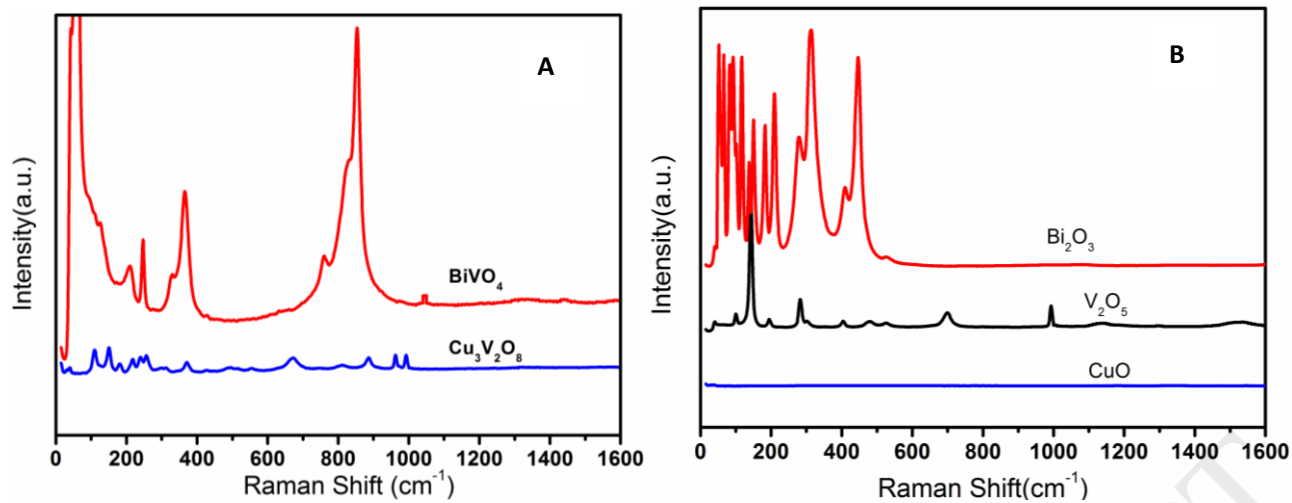


Fig. 3

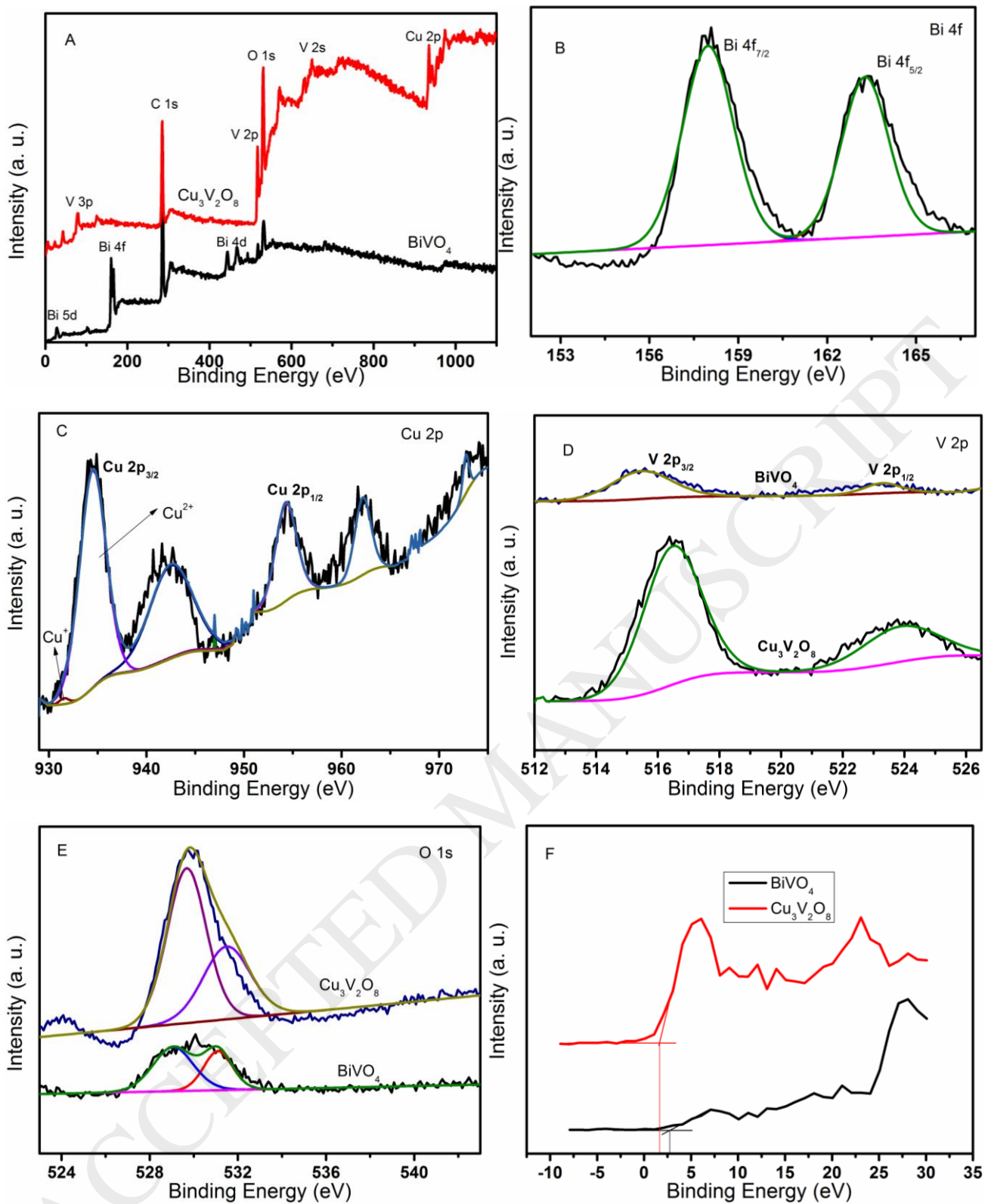


Fig. 4

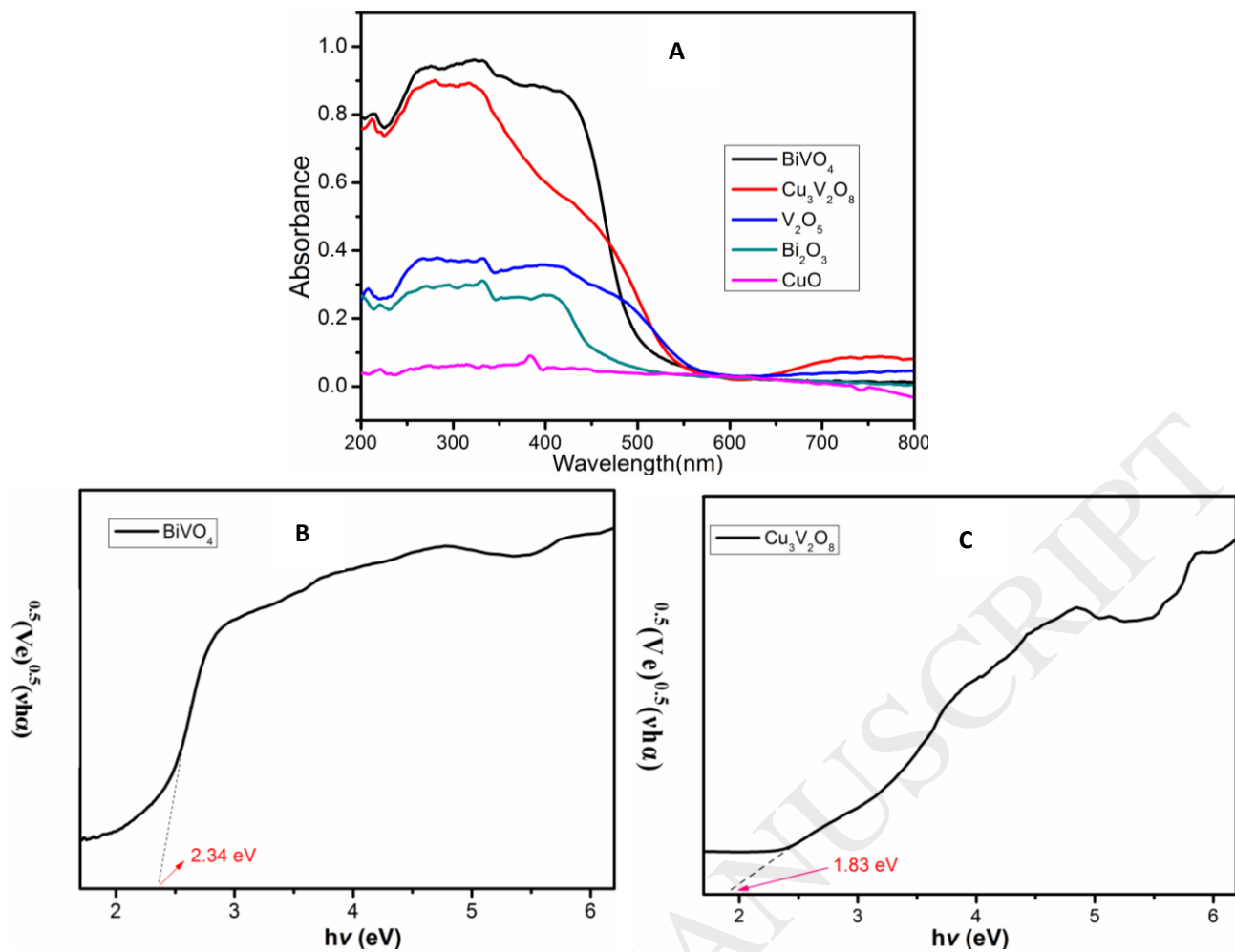


Fig. 5

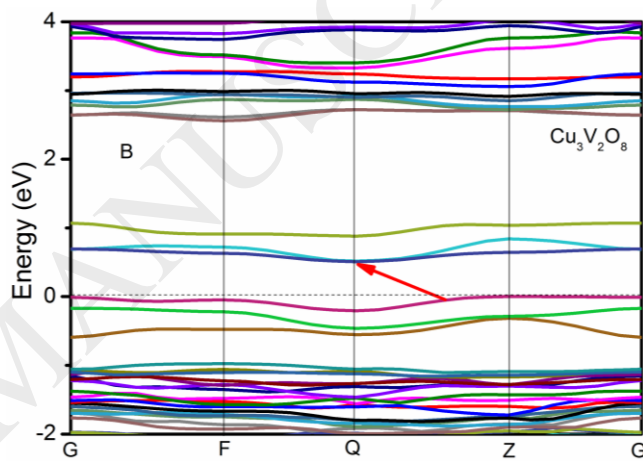
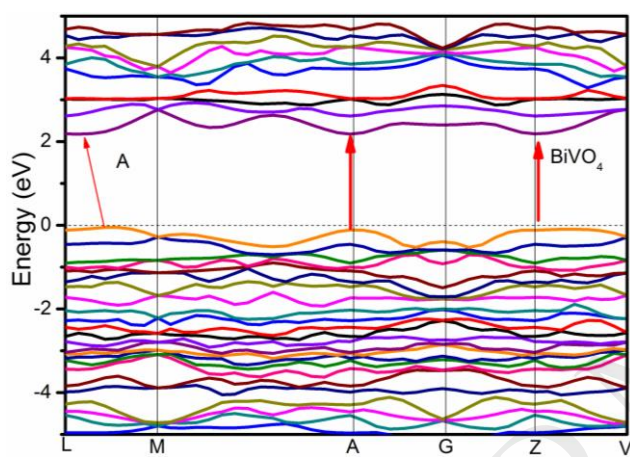
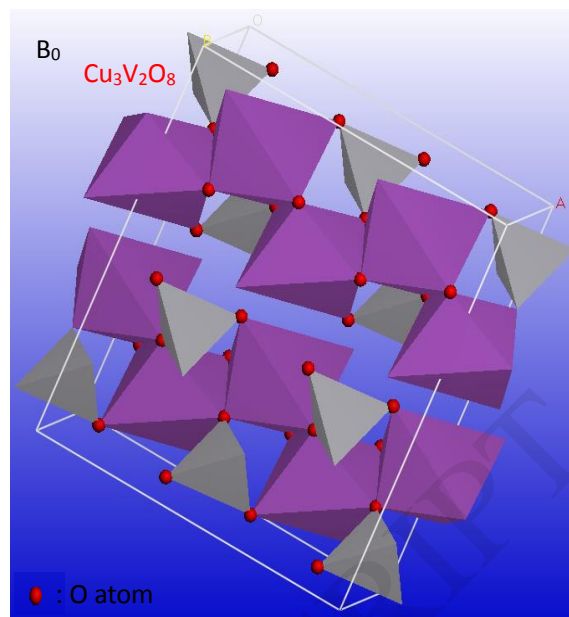
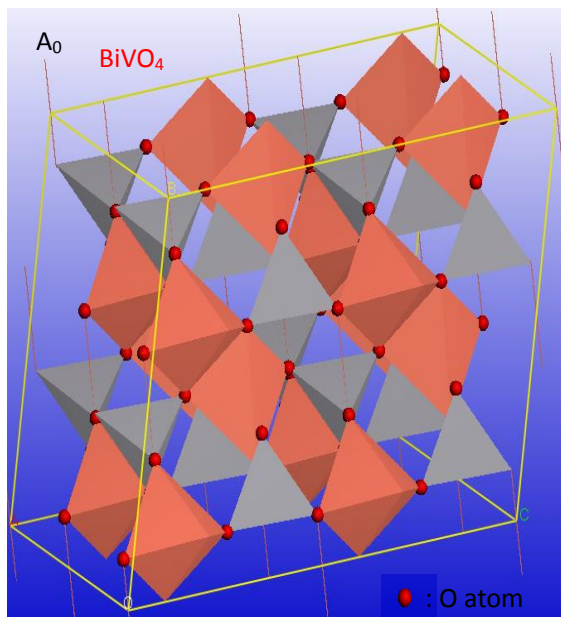


Fig. 6

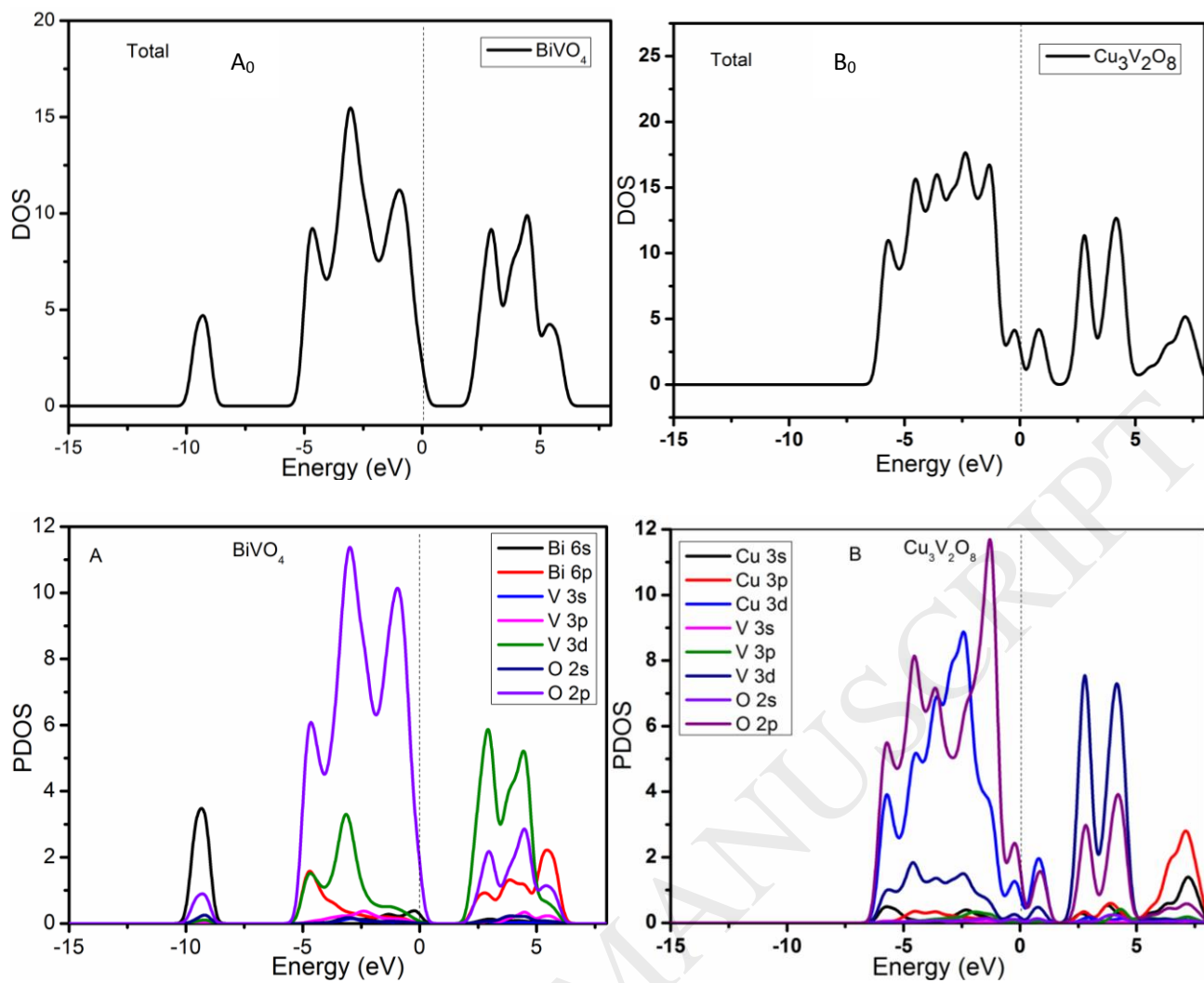


Fig. 7

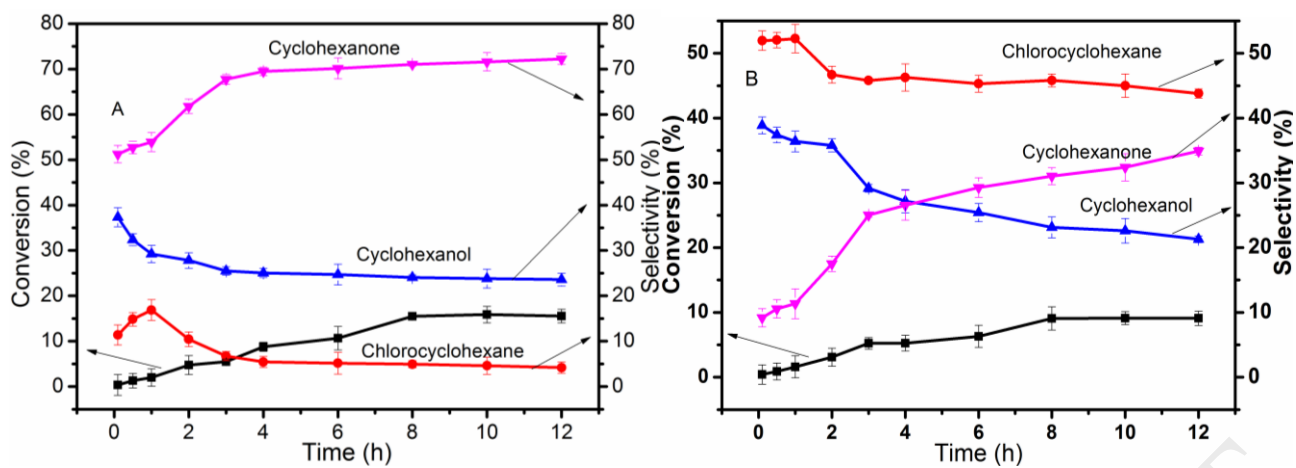


Fig. 8

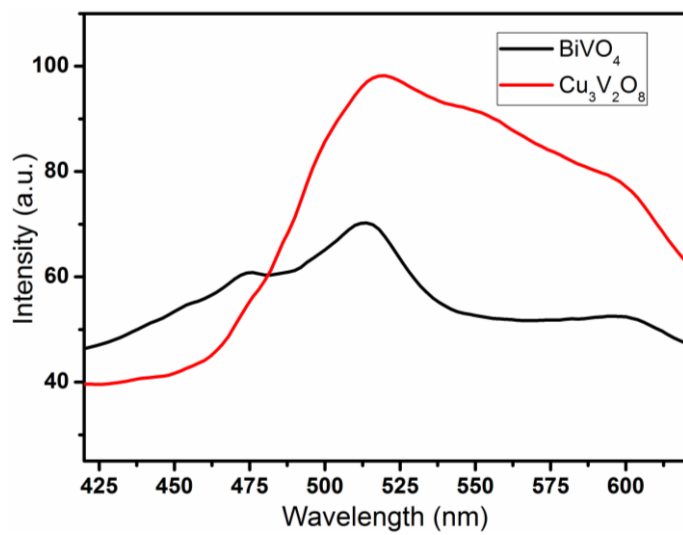


Fig. 9

ACCEPTED MANUSCRIPT

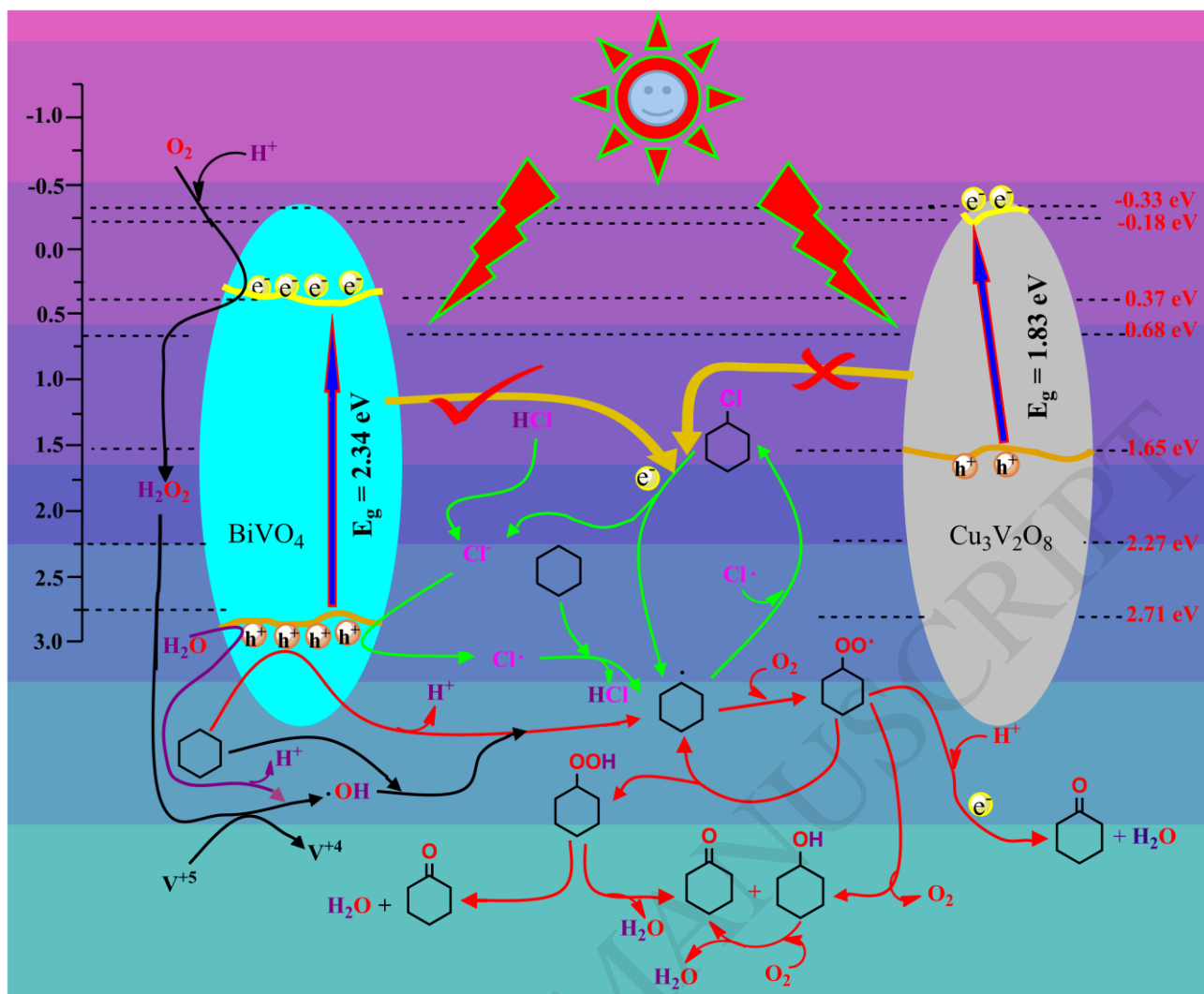


Fig. 10